



Università
Ca' Foscari
Venezia

Master's Degree
in

Science and Technology of Bio and
Nanomaterials

MODIFIED NANOSTRUCTURED BISMUTH FERRITE THIN FILMS FOR APPLICATIONS IN PHOTOELECTROCATALYSIS

Supervisor

Prof. Adolfo Speghini

Co-Supervisor

Dr Joe Briscoe

MSc Student

Chiara Cressoni
871816

Academic Year

2018 / 2019

Abstract

The thesis project is focused on the synthesis and characterization of nanostructured bismuth ferrite, BiFeO_3 (BFO), thin films with enhanced photoelectrocatalytic properties. Photoelectrocatalytic materials are semiconductors that are able to catalyze water splitting processes or other reactions under sunlight irradiation. They can, through the absorption of photons, create electron/hole pairs which can be exploited to carry out electrochemical reactions. BFO is a very promising perovskite-type material with an optical band gap that fits well with the sunlight irradiation in the visible region. Since most conventional photocatalysts like TiO_2 are limited by a wide band gap and a UV light absorption, the BFO material is an interesting visible light driven photoactive material for solar energy conversion. The main disadvantages of such material are poor efficiency and high variability in the photoelectrocatalytic performance. BFO's performance depends on structure, defects, phase, electronic properties, which are directly connected with the synthetic methodology. In this thesis a sol-gel synthesis has been optimized in order to prepare highly reproducible thin films, that could be directly applied to a device, with modified structure and improved photoelectrocatalytic performance. Moreover, in order to achieve sensitization in the Near Infrared Region where pure BFO is not active, a composite nanomaterial has been developed. Previously prepared nanoparticles with peculiar optical properties have been dispersed in a BFO matrix and the optical and structural characterization have been carried out to correlate the enhancement of photoelectrocatalytic properties with the modification caused by the nanoparticles doping.

INDEX

Abstract	
TABLE INDEX	II
FIGURE INDEX	II
1 INTRODUCTION.....	1
1.1 Photovoltaic and Photocatalysis	1
1.2 Semiconductors	3
1.3 Nanotechnologies, nanoparticles and nanocomposites	5
1.4 Perovskite-type materials and Bismuth Ferrite	7
1.5 Sol-gel synthesis of thin films	9
1.6 Lanthanide-doped Upconverting Nanoparticles (UCNPs).....	10
1.7 Energy transfers and upconversion.....	13
1.8 Aim of the thesis	15
2 CHARACTERIZATION TECHNIQUES	17
2.1 X-Ray Diffraction.....	17
2.2 Electron Microscopy	18
2.3 Spectroscopy	21
2.3.1 UV-Vis absorption spectroscopy and Tauc plot.....	22
2.3.2 Laser spectroscopy	22
2.4 PEC analysis	23
3 EXPERIMENTAL PART	25
3.1 Reagents	25

3.2 Synthesis of Bismuth Ferrite thin films.....	25
3.3 Synthesis of Upconverting Nanoparticles.....	28
3.4 Synthesis of nanocomposite	29
4 RESULTS AND DISCUSSION	30
4.1 Optimization of synthesis protocol of BFO	30
4.2 Characterization of Upconverting Nanoparticles	40
4.3 Characterization of BFO-UCNPs nanocomposite.....	44
5 CONCLUSIONS.....	52
6 BIBLIOGRAPHY	55

TABLE INDEX

Table 1. Reagents used for preparation of sol precursor of BFO.	25
Table 2. Reagents used for preparation of SrF ₂ :Yb,Tm nanoparticles.....	28
Table 3. Reagents used for preparation of CaF ₂ :Yb,Er nanoparticles.....	28

FIGURE INDEX

Figure 1 A schematic illustration of the formation of photogenerated charge carriers upon absorption of radiation. The generated electron-hole pairs can react with water and carry out water splitting.	2
Figure 2. A simplified mechanism for organic pollutants degradation by a photocatalyst.	3
Figure 3. A band gap diagram showing the different sizes of band gaps for conductors, semiconductors, and insulators.....	3
Figure 4. Scheme of the position of Fermi level in p- and n-type semiconductors.....	4
Figure 5. Nanomaterials classifications according to the length scale of each dimension. Nanomaterials can be nanoscaled in three (3D), two (2D), one (1D) or zero (0D) dimensions. Examples of each one of the categories are also reported in the image.	6
Figure 6. Scheme of the ABX ₃ perovskite type structure.	7
Figure 7. Schematic diagram of the crystal structure of bismuth ferrite BiFeO ₃	8
Figure 8. Preparation of different structures via the sol-gel method.	10
Figure 9. Lanthanides orbitals diagram and distance from the nucleus. The shielding of 4f orbitals by the more external shells is clearly shown.....	11
Figure 10. Simplified Dieke diagram of energy levels of lanthanide ions in LaCl ₃ host lattice.	12
Figure 11. Schematic diagram of the ETU process.	13
Figure 12. Energy level diagrams of (a) NaYF ₄ :Yb ³⁺ ,Er ³⁺ and (b) NaYF ₄ :Yb ³⁺ ,Tm ³⁺ . Solid, dotted and wavy arrows represent photon absorption or emission, energy transfer and relaxation processes, respectively. The blue wavy arrows denote the increased multiphonon relaxations caused by OH vibrations.	14

Figure 13. Schematic illustration of spectral overlap of the absorption of BFO (pink) and emission of the UCNPs (blue).	16
Figure 14. A two-dimensional crystal lattice and a set of imaginary planes is represented by the grid. X-rays incident on the crystal at an angle θ produce coherent diffraction when the difference in the travelled distance is equal to an integer multiple of the wavelength.....	17
Figure 15. Scheme of the fundamental steps in a diffraction experiment.....	18
Figure 16. Image of the different signals that can be detected in the SEM analysis.	19
Figure 17. A general scheme of the scanning electron microscope and its principal components.	20
Figure 18. Energy states of a diatomic molecule. The curves represent the electronic energy levels; the lines marked are the vibrational levels inside each electronic level. Between two vibrational levels there are the rotational modes.	21
Figure 19. Scheme showing the setup for the emission experiment in backscattering mode.	23
Figure 20. Schematic illustration of the three-electrode setup used to carry out photoelectrochemical analysis.	24
Figure 21. Linear potential sweep as a function of time.	24
Figure 22. Bismuth ferrite precursor solution.	26
Figure 23. The G3P spincoat.	26
Figure 24. BFO thin films (1 layer) deposited on FTO substrate, before the annealing step.....	27
Figure 25. BFO samples deposited on FTO glass substrate from the same precursor solution at different aging times.	30
Figure 26. SEM image of BFO sample at day 1 (left) and respective current density acquired by performing Linear Sweep Voltammetry experiment (right).....	31
Figure 27. SEM image of BFO sample at day 2 (left) and respective current density acquired by performing Linear Sweep Voltammetry experiment (right).....	31
Figure 28. SEM image of BFO sample at day 3 (left) and respective current density acquired by performing Linear Sweep Voltammetry experiment (right).....	32
Figure 29. SEM image of BFO sample at day 4 (left) and respective current density acquired by performing Linear Sweep Voltammetry experiment (right).....	32

Figure 30. SEM image of BFO sample at day 5 (left) and respective current density acquired by performing Linear Sweep Voltammetry experiment (right).....	33
Figure 31. SEM image of BFO sample at day 5, 1 layer (left) and respective current density acquired by performing Linear Sweep Voltammetry experiment (right).	34
Figure 32. SEM image of BFO sample at day 5, 3 layers (left) and respective current density acquired by performing Linear Sweep Voltammetry experiment (right).	34
Figure 33. SEM image of BFO sample at day 5, 5 layers (left) and respective current density acquired by performing Linear Sweep Voltammetry experiment (right).	35
Figure 34. SEM image of BFO sample at day 5, 1 layer, oxygen atmosphere (left) and respective current density acquired by performing Linear Sweep Voltammetry experiment (right).....	36
<i>Figure 35. The chop curves for samples at different aging times are compared in the left image. The current density at 0 V vs. NHE is plotted against the aging time of the precursor solution to show the increasing in performance (right).</i>	<i>36</i>
Figure 36. UV-Vis absorption spectrum of BFO thin film synthesized at day 5, 1 layer, in air atmosphere.....	37
Figure 37. Tauc plots showing the direct (left) and indirect (right) band gaps of the BFO thin film.	37
Figure 38. Raman spectrum of BFO thin film.....	38
Figure 39. Raman spectra of BFO taken from literature, showing similar peaks to the experimental ones in the region between 100 and 250 cm^{-1}	38
Figure 40. X-ray diffraction pattern of FTO glass substrate (blue) and pure BFO deposited on the glass substrate (black).	39
Figure 41. TEM images of CaF_2 nanoparticles showing spherical morphology and good monodispersity.	40
Figure 42. X-rays diffraction pattern of $\text{SrF}_2:\text{Yb},\text{Tm}$ NPs.....	41
Figure 43. X-rays diffraction pattern of $\text{CaF}_2:\text{Yb},\text{Er}$ NPs.....	41
Figure 44. Upconversion emission spectrum of NPs: Yb^{3+} , Er^{3+} under 980 nm laser irradiation. The inset on the upper right shows the energy level diagram for the energy transfer.....	42
Figure 45. Upconversion emission spectrum of NPs: Yb^{3+} , Tm^{3+} under 980 nm laser irradiation.	43

Figure 46. Image showing the nanocomposites prepared at different days, with the respective BFO control.....	44
Figure 47. Linear Sweep Voltammetry experiment on pure BFO sample deposited at day 1 of aging of precursor solution.....	45
Figure 48. Generated photocurrent (left) and SEM image (right) for the sample of nanocomposite BFO+UCNPs prepared at day 1.	45
Figure 49. Generated photocurrent (left) and SEM image (right) for the sample of pure BFO prepared at day 5.	46
Figure 50. Generated photocurrent (left) and SEM image (right) for the sample of nanocomposite BFO+UCNPs prepared at day 5.	46
Figure 51. Overlapped curves of pure BFO samples and nanocomposite, showing the increasing in PEC performance.	47
Figure 52. UV-Vis absorption spectrum of nanocomposite. The insets show the Tauc plot for direct (above) and indirect (below) band gap.....	48
Figure 53. XRD pattern of nanocomposite (red line) of BFO thin film with calcium fluoride UCNPs.....	49
Figure 54. Multiphoton Laser Scanning Microscope images of pure BFO thin film (left) and nanocomposite BFO+CaF ₂ :Yb,Er (right). Excitation: 980 nm; emission: visible range (400-700 nm).	50
Figure 55. The acquisition of luminescence from the sample is divided into three different ranges, each one corresponding to a portion of the visible spectrum.	50

1 INTRODUCTION

1.1 Photovoltaic and Photocatalysis

Our ancestors worshipped the sun as a god and as a life-giver planet. Later in the centuries, with the improvement of the scientific and technologic knowledge, we were able to understand the real importance of the Sun as a source of energy for every living organism on Earth. But the full awareness of the importance of the sun has been reached only in the current era, when the extraction of fossil fuels has been proven to irreparably damage our planet.

Furthermore, from the industrial revolution on, the technologies and industries have grown and the quantity of emissions of greenhouse gases have reached dangerous levels. Such emissions and the directly correlated consequences will cause in the next years droughts, floods, sea level rise, glacier melting and serious damages to agriculture and natural ecosystems. This needed reduction of greenhouse gases emissions can be achieved by moving from the traditional energy sources to renewable ones.¹

Renewable energy sources are defined as “energy obtained from the continuous and or repetitive currents on energy recurring in the natural environment” or also as “energy flows which are replenished at the same rate as they are used”.² All the Earth’s renewable energy sources derive from solar energy, which can be converted using various technologies. The sunlight arrives as white light since it is composed of a wide spectrum of wavelengths, going from the infrared to the ultraviolet radiation. The direct conversion of solar radiation into electricity is called photovoltaic effect (PV).

This process can be carried out by means of a photovoltaic (PV) device. Instead, a photoelectrochemical (PEC) cell is a device which converts the solar energy into chemicals and its functionality is based on the behavior of the interface between a semiconductor and an electrolyte.³ A particular kind of PEC cell is the dye-sensitized solar cell (DSSC), which converts sunlight directly to electricity (via the use of a redox shuttle).

Not only energy, but also renewable fuels are promising alternatives to the fossil fuels for production of energy. H₂ has been identified as one of these potential innovative fuels,

that produces a high energy yield and it is pollution free. The disadvantage is that its production is currently based on petroleum and natural gas steam reforming, making this process no more sustainable on long term.

In recent years, there has been growing interest in the development of new technologies for carrying out this process in a more environmental-friendly way. The photocatalytic water splitting is a process that exploits solar energy for catalyzing the process of hydrogen production.⁴ Hydrogen production via water splitting with a TiO₂ photocatalytic device was first reported by Fujishima and Honda.⁵ The basic principle on which a photoelectrochemical cell relies is that light absorption generates electron-hole pairs on the photoanode and this triggers the reactions that will produce the water splitting. In particular, photo-generated holes catalyze the oxidation of water at the anode surface, with production of O₂ and H⁺, while photo-generated electrons are transferred to the cathode and these electrons are finally used for the reduction of H⁺ on the surface of the photocathode to produce H₂, as shown in Fig. 1.

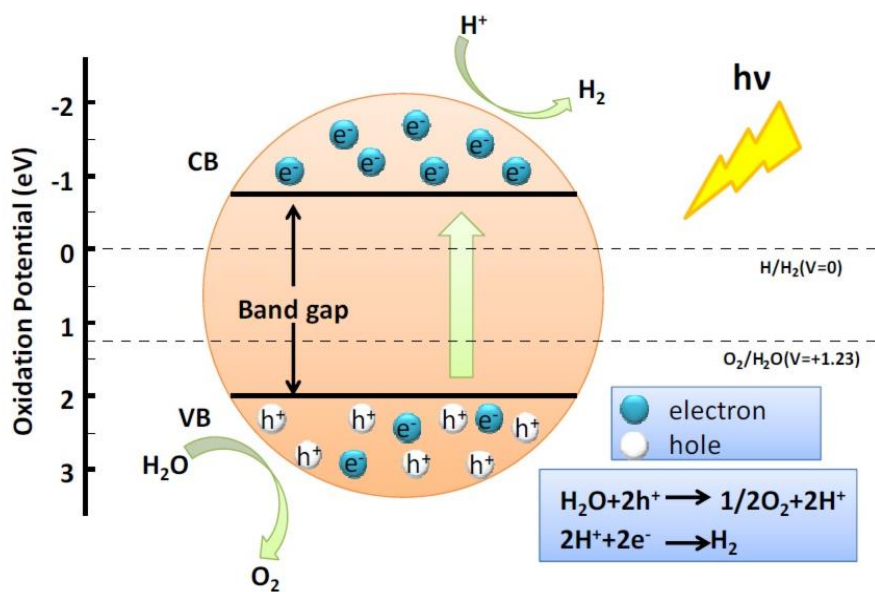


Figure 1. A schematic illustration of the formation of photogenerated charge carriers upon absorption of radiation. The generated electron-hole pairs can react with water and carry out water splitting.¹⁸

Moreover, semiconductor heterogeneous photocatalysis has enormous potential to treat organic contaminants in water and air. Traditional water treatment methods based on adsorption, coagulation or membrane separation, suffer from high operating costs and low efficiency or production of secondary pollutants. Semiconductor photocatalysts have

shown good efficiency in degrading a wide range of organic pollutants into biodegradable or less toxic compounds, as CO_2 , H_2O , NO_3^- , PO_4^{3-} , and halide ions.⁶

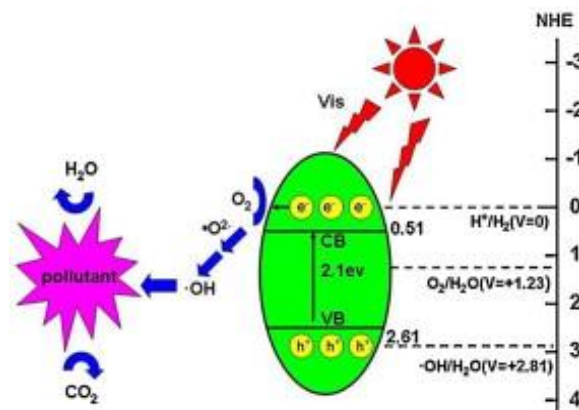


Figure 2. A simplified mechanism for organic pollutants degradation by a photocatalyst.

1.2 Semiconductors

A semiconductor material is defined as a material whose band gap is sufficiently small to permit the presence of electrical conductivity. In general, its resistance decreases by increasing the temperature and the conductivity is affected by the presence of impurities inside the crystal structure.

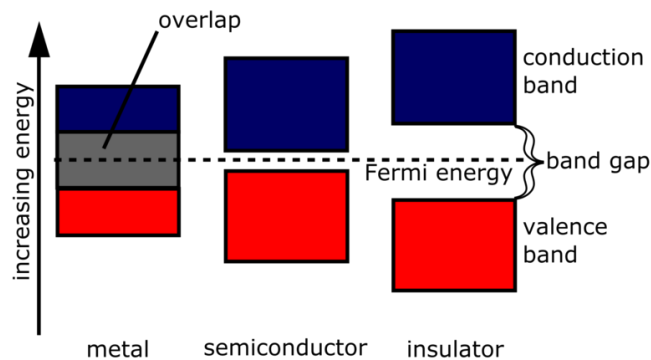


Figure 3. A band gap diagram showing the different sizes of band gaps for conductors, semiconductors, and insulators.³⁹

When in the same crystal two differently doped regions are present, a semiconductor junction is found. The behavior of charge carriers at these junctions is the basic principle of the functioning of all the semiconductor devices. The understanding of semiconductor properties is based on quantum physics, able to explain the movement of charged particles within the crystal lattice. The most important charge carriers in semiconductors

are electrons and holes, that are free to move producing the typical electric properties. A semiconductor which contains mostly free holes is called p-type, when it contains mostly free electrons it is a n-type semiconductor. The boundary region between the two different type of semiconductors is called p-n junction and it is responsible for the electronic behavior of these materials.



Figure 4. Scheme of the position of Fermi level in p- and n-type semiconductors

The properties of semiconductors depend on the quantum states of the electrons in the material and on the electronic band structure associated to it. Electrical conductivity is generated by delocalized electrons and the movement of charges is due to partially filled nature of the quantum states. A state that is partially filled means that its energy is close to the Fermi level, defined as the thermodynamic work required to add an electron to the body. A material possesses high conductivity when it has many delocalized electrons and many partially filled states. Metals are for example good conductors because they have many partially filled states with energy close to the Fermi level. On the contrary, insulators have few partially filled states and they have wide band gaps, where no electron states can exist. Since a semiconductor has a band gap which is smaller than that of an insulator, at room temperature a significant number of electrons can be excited, for example by absorbing photons, and cross the band gap. The band of the states that is beneath the band gap is called valence band and the band of states above the band gap is called conduction band. They are the bands that are closest to the energy of the Fermi level and they determine the electrical behavior of the solid.

Semiconductor materials are used as basis for the development of photoelectrochemical cells, thanks to their ability to generate electrons and holes. Semiconductor photocatalysts behavior depends on the difference between the Fermi levels of the photoanode and the photocathode. When the semiconductor is hit by light, it absorbs a

photon and if the energy of the photon is equal or exceeds the band gap energy, an electron is promoted from the VB to the CB, leaving a hole in the valence band. Photogenerated electrons and holes are sometimes able to reduce and oxidize water or other organic molecules, respectively, as explained in the previous paragraph 1.1.⁷

In general, the electron-hole pairs migrate on the surface of the semiconductor, where they can promote reactions. Surface recombination is a competing pathway occurring on the surface and sometimes decreasing the efficiency of photocatalysis.

Semiconductors offer a variety of applications in many fields, from the renewable energy generation, to water splitting and organic pollutants degradation, from biosensors and biotissue generation to therapeutic treatment of cancer and viral infections and pharmaceutical industry.^{8,9}

1.3 Nanotechnologies, nanoparticles and nanocomposites

Nanomaterials are defined as compounds with at least one dimension that lies in the range 1-100 nm.¹⁰ Nanotechnology is the field of the research that studies development, synthesis, characterization and applications of nanomaterials. Nanomaterials and nanoparticles could have different size, shape and composition from gold nanorods to carbon nanotube and also metallo-organic nanocages or ferro-magnetic nanospheres. There are many synthetic methods and nanochemistry plays a critical role in regulating the nanomaterial synthesis to obtain peculiar physical and chemical features.

Nanoparticles have several unique properties which are completely different from their bulk counterparts and often their properties are in the middle between that of the atoms or molecules and that of the macroscopic materials. Nanomaterial properties differ from their bulk counterparts mainly due to changes in physical features such as size, shape and surface area and quantum effects such as quantum confinement. Quantum confinement is defined as the organization of energy levels that is observed when the size of the material is of the same magnitude as the De Broglie wavelength of the electron.

Some of the most important features of nanomaterials are the high surface-to-volume ratio and high surface energy, together with peculiar thermal, optical, electrical

properties. Their chemical reactivity as well as their dispersibility can be regulated with functionalization of the surface or changing the synthetic parameters. For their wide variety of properties, nanomaterials can be applied in several field, like electronics, energy harvesting and storage, biology, medicine or pharmacology.¹¹

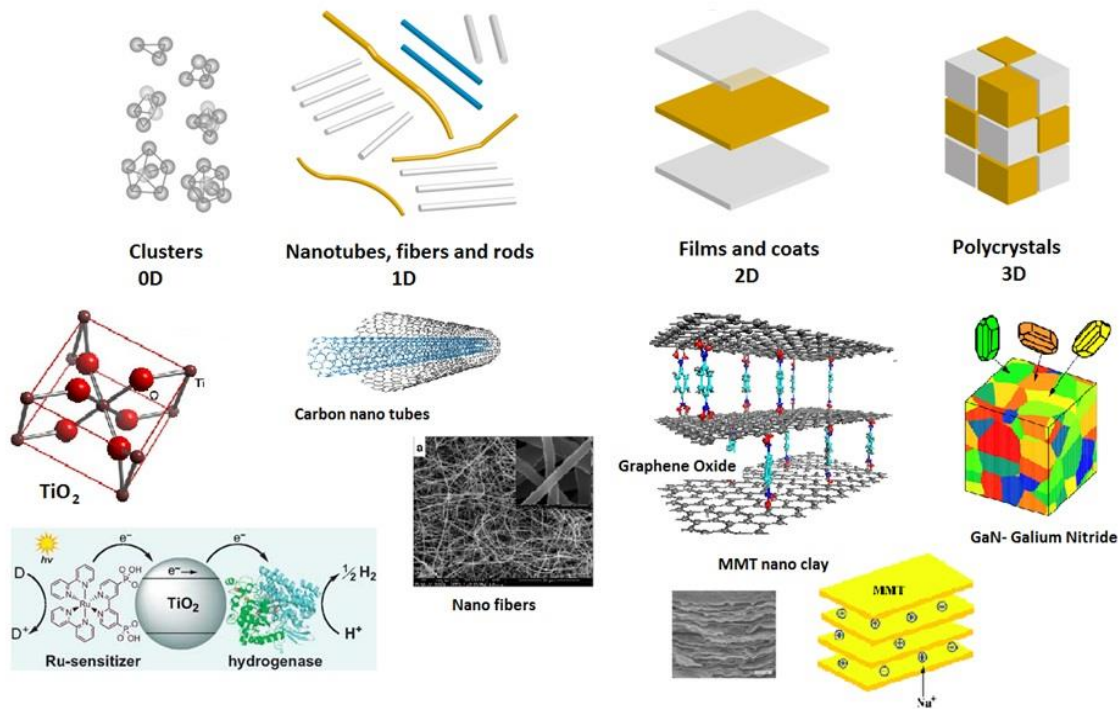


Figure 5. Nanomaterials classifications according to the length scale of each dimension. Nanomaterials can be nanoscaled in three (3D), two (2D), one (1D) or zero (0D) dimensions. Examples of each one of the categories are also reported in the image.

The advantage of nanotechnology is the ability to control the material at the atomic scale and this can be used also for incorporating nanoparticles in a macroscopic matrix and create a new class of materials with additional and different properties.

Nanocomposites are heterogeneous multiphase materials in which one or more of their phases have sizes at the nanoscale. The basic concept to describe nanocomposites is to build highly controlled nanometric building blocks and assemble them into materials with new and different physical and chemical properties. Nanocomposites are present in nature, for example in minerals, in shells of invertebrates and also in bone, conferring resistance and strength to the original matrix.¹² They are also already used in industrial practice, incorporating nanoparticles in different material, providing properties such as conductivity, magnetism, permeability, UV protection, optical response, catalytic activity, biodegradability.

1.4 Perovskite-type materials and Bismuth Ferrite

Perovskite-type materials are a class of mineral compounds with the same type of crystal structure of calcium titanite (CaTiO_3), known as perovskite structure. Their name derives from the Russian mineralogist L. A. Perovski. The general chemical formula is written as ABX_3 , where A and B are two cations of very different sizes, respectively large and small cation, and X is an anion that is bound to both.

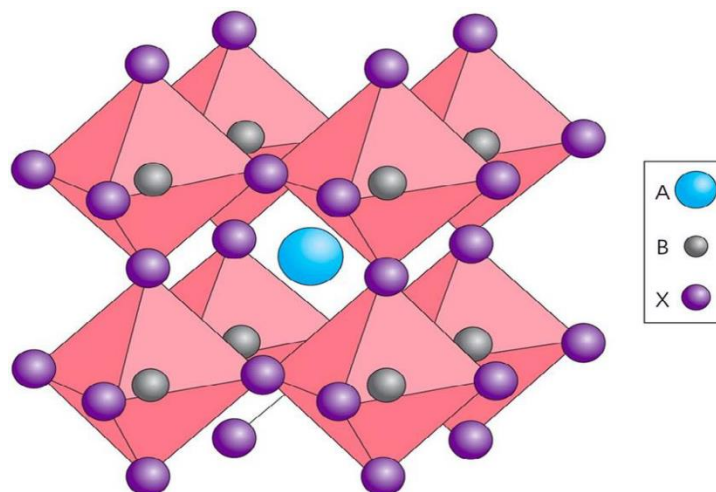


Figure 6. Scheme of the ABX_3 perovskite type structure.

The perovskite structure is adopted by many oxide materials that have the general formula ABO_3 . These isomorphous solids are quite interesting for their versatility, due to the flexibility in chemical composition, with many different cations that can fit into A and B positions, within the same crystal structure. Perovskites have been widely explored also for their high thermal stability, the excellent oxidation activity and low price, mainly for environmental applications.¹³ Perovskite-type materials usually possess also superconductivity, magnetoresistance and other dielectric properties. For all these reasons they have been investigated for applications in photovoltaic and photoelectrocatalysis, such as sunlight-driven water electrolysis.¹⁴

Common examples of perovskite-types materials are strontium titanate (SrTiO_3), lead titanate (PbTiO_3), lanthanum ytterbium oxide (LaYbO_3) and bismuth ferrite (BiFeO_3).

These compounds can be used as sensors and catalyst electrodes in certain types of fuel cells like PEC cells and are also promising candidates for memory devices and spintronics applications.¹⁵

Perovskites compounds could be also brought to nanoscale size, synthesizing nanoparticles, nanorods, nanowires with new interesting properties and high control of size and shape, increasing the applications in devices and technologies.¹⁶

In fact, when compared with the analogue bulk materials, these perovskite nanoparticles have higher photocatalytic performance due to their larger surface area and higher catalytic activity, but their active life is short due to their instability and tendency to aggregate in bigger particles.

Bismuth ferrite, also referred as BFO, is an inorganic chemical compound with perovskite structure and with very interesting multiferroic behavior.¹⁷ Materials that possess at the same time electric, magnetic, and structural order parameters that result in simultaneous ferroelectricity, ferromagnetism and ferroelasticity are known as multiferroics. At room temperature the BFO has rhombohedral phase, belonging to the $Rc3$ space group. In addition to its magnetic and electric properties, this material also possesses photovoltaic applications, involved in the so-called ferroelectric photovoltaic effect.

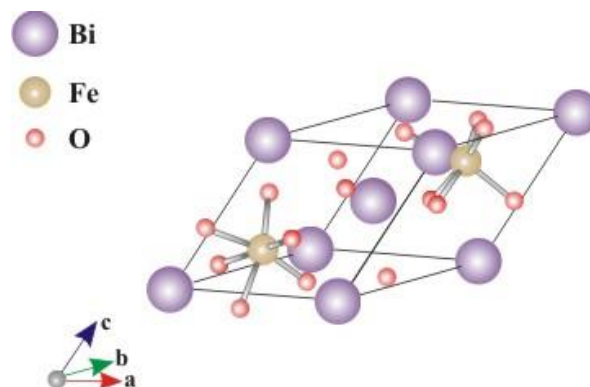


Figure 7. Schematic diagram of the crystal structure of bismuth ferrite BiFeO_3 .

Recently bismuth ferrite has attracted much interest for solar applications due to its narrower band gap (2.1-2.7 eV) compared with other commonly used semiconductors like TiO_2 , allowing a photocatalytic activity under the visible light irradiation.

The electrical polarisation occurring in BiFeO_3 -based materials may reduce the recombination of the photogenerated charged carriers during the transmission process that usually occurs in the photoelectrocatalysts and this can further increase the quantum efficiency. Therefore, BFO can serve as a promising photocatalyst either for hydrogen generation from water splitting or for degradation of organic pollutants in the future.¹⁸

The bismuth ferrite is not found in nature, so different synthetic routes have been developed. In particular, the synthesis into epitaxial thin films has the great advantage that they can be directly incorporated into devices and their thickness could also lie in the nanometric range.

1.5 Sol-gel synthesis of thin films

The sol-gel synthesis is a well-established bottom-up approach for synthesis of solid materials starting from molecular precursors. It is commonly used for the preparation of oxides and perovskite materials in different sizes and shapes. The mechanism involves a first step of formation of a liquid “sol”, usually containing colloidal nanoparticles, that condenses into a solid phase, the “gel”. In a typical sol-gel process, the precursor is subjected to a series of hydrolysis and polymerization reactions to form a colloidal suspension (“sol”). Further processing of the "sol" makes it possible to make materials in different forms such as: monolith, films, fibers, and nanosized powders.¹⁹ The advantages of sol-gel synthesis are the good control of stoichiometry in precursor solutions, the ease of compositional modification, the possibility to tune the size and shape of the final compound, the possibility to introduce additional components or functional groups, to cover large surfaces and the capability to use simple and cheap equipment.

Regardless the desired structure of the material, the synthesis usually starts with a precursor solution that is composed by a metal source, a solvent and a chelation agent.²⁰

Because of the liquid nature of the precursor, the final material can be fabricated in a variety of morphologies simply by “casting” the precursor into an appropriate template or by using different deposition approaches. For example, spin-coating method is used for thin films deposition, nanowires and nanotubes are formed by pouring into templates and electrospinning is used to obtain nanofibers (see Fig. 8).

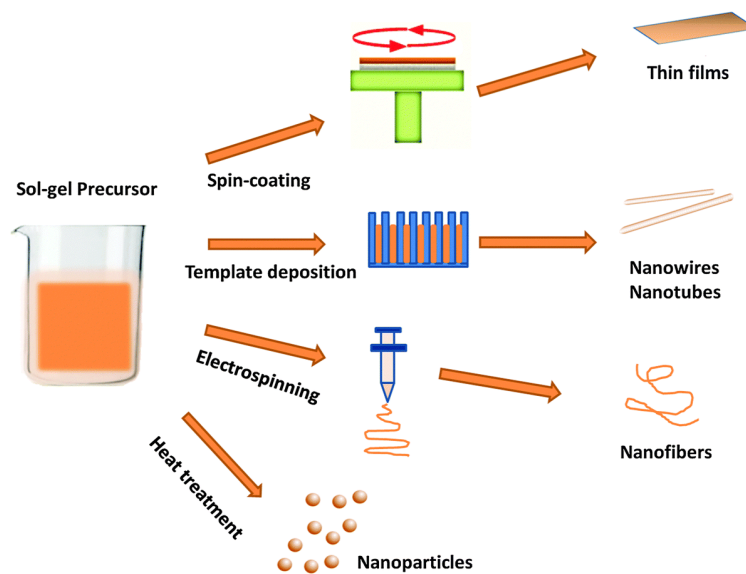


Figure 8. Preparation of different structures via the sol-gel method.

In the original sol-gel method the metal alkoxides in water are used as metal precursors. However, metal alkoxides are quite expensive, so they could be substituted by metal salts like metal nitrates or chlorides in an organic solvent like 2-methoxyethanol (2-MOE) and ethylene glycol (EG) for the synthesis of perovskite materials. Such solvents are chosen for the good solubility of other reagents in them and because their linear structure is also believed to help the formation of dense and stable precursor solution. Chelating agents such as acetic anhydride, acetic acid, citric acid, or tartaric acid, are used to chelate the metals and facilitate the gelation process under certain reaction conditions. The molecular structure of chelating agent affects the solution viscosity and nanoparticles growth during film formation.

1.6 Lanthanide-doped Upconverting Nanoparticles (UCNPs)

Lanthanide-doped UCNPs are nanosized systems where suitable trivalent lanthanide ions are accommodated in a crystal host.

Lanthanides are 4f elements that possess similar chemical properties. Together with Scandium and Yttrium, lanthanides are also named as Rare-earth elements (IUPAC). The valence electrons of lanthanides are in 4f orbitals, shielded by the electrons in more external orbitals, as 5s, 5p and 6s. This shielding of the 4f electrons, makes them poorly

perturbed by the local crystal field around the ion and the electronic configuration can be described by the free ion approximation.²¹

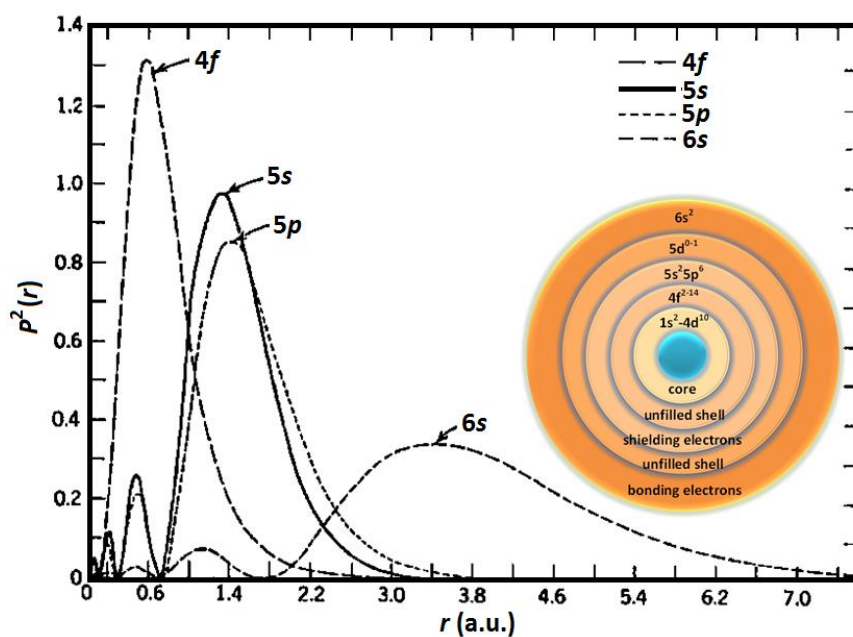


Figure 9. Lanthanides orbitals diagram and distance from the nucleus. The shielding of 4f orbitals by the more external shells is clearly shown.

The energy levels for Ln^{3+} ions as dopant in LaCl_3 host are shown in Figure 10 (Dieke diagram).²² In the Dieke diagram the levels are labelled as $^{2S+1}L_J$, known as spectroscopic term, where L is the total orbital momentum which can assume integer values (0,1,2,3,4,...) corresponding to different letters (S,P,D,F,G,...), S is the total spin momentum and J is the total angular momentum of the level. The energy levels can be also split in several Stark states,²³ according to the Kramers degeneracy. Although the Laporte's selection rule applies for spectroscopic transitions involving 4f electrons, many transitions are observed (absorptions and emissions) due to mixing of states of different parity in the crystal host.²²

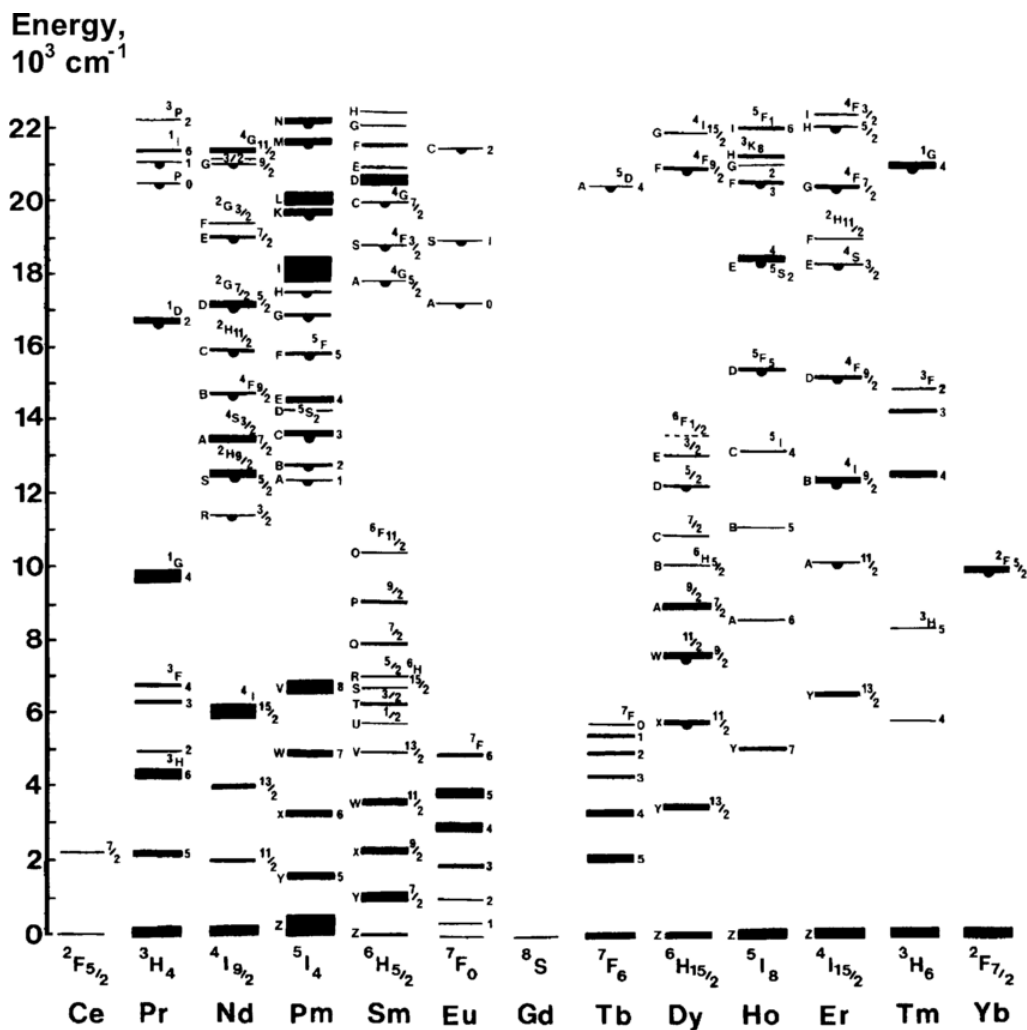


Figure 10. Simplified Dieke diagram of energy levels of lanthanide ions in LaCl_3 host lattice.

Therefore, the absorption and the emission bands of Ln^{3+} ions correspond to the transitions between energy levels described in the diagram. Usually the bands are quite sharp because of the shielding effect of $4f$ electrons and they are characterized by long lifetimes, in the ms- μs range. The lanthanide ions have characteristic emission bands that are poorly dependent by the matrix size. The emission properties make them interesting for different applications, from the biomedical field to electronics and optical diodes.²⁴

Typical host lattices for lanthanide-doped UCNP are oxide or fluoride-based, with low phonon energy cutoffs ($< 400 \text{ cm}^{-1}$) and low non-radiative decay probability, that increases the efficiency of the radiative processes. Lattice hosts also should have suitable sites to accommodate the Ln^{3+} dopants. For optical applications, they also should have low absorption in the spectral region of interest and they should possess high chemical and physical stability.

1.7 Energy transfers and upconversion

One interesting spectroscopic property related to the energy levels of lanthanide ions is the ability to carry out the upconversion process (UC). Upconversion is an energy transfer mechanism in which the absorption of one or more photons generates the emission of photons with higher energy, also called anti-Stokes process. This kind of energy transfer is the opposite of Stokes emissions from luminescent nanoparticles, where photons of lower energies are produced by radiation excitation at a given energy. Lanthanide ions can be involved in both Stokes luminescent nanoparticles and in anti-Stokes UCNPs.²⁵ The upconversion energy transfer usually occur through energy transfer upconversion (ETU), which involves two lanthanide ions. This is among the more efficient UC processes and its efficiency depends on the distance between the Ln^{3+} dopants and therefore on their concentration.

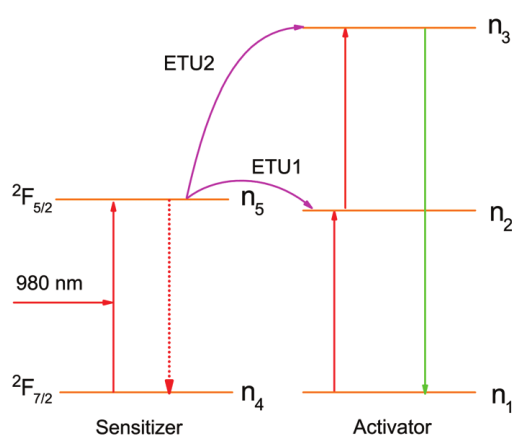


Figure 11. Schematic diagram of the ETU process.

Among the lanthanide ions involved in the UC process, it is possible to distinguish the sensitizer, which is directly excited by the incident radiation, and the activator, which receives the energy from the sensitizer and generates the UC emission.²⁶ Normally the sensitizer is present in relatively high concentration, around 20% with respect to the total metal ions, while the activator concentration is usually less than 2%, in particular to avoid cross-relaxation deactivation between emitting ions.

Commonly used UC couples are $\text{Yb}^{3+}\text{-Tm}^{3+}$ with emission in the blue and red region of visible light and $\text{Yb}^{3+}\text{-Er}^{3+}$ for an emission in the green and red region. A laser radiation at 980 nm directly excites the Yb^{3+} sensitizer ion from the ${}^2F_{7/2}$ ground state to the ${}^2F_{5/2}$

excited state. The sensitizer absorbs more than one photons and transfers the energy to the activator ions,²⁷ Tm^{3+} or Er^{3+} , as shown in Figure 12.

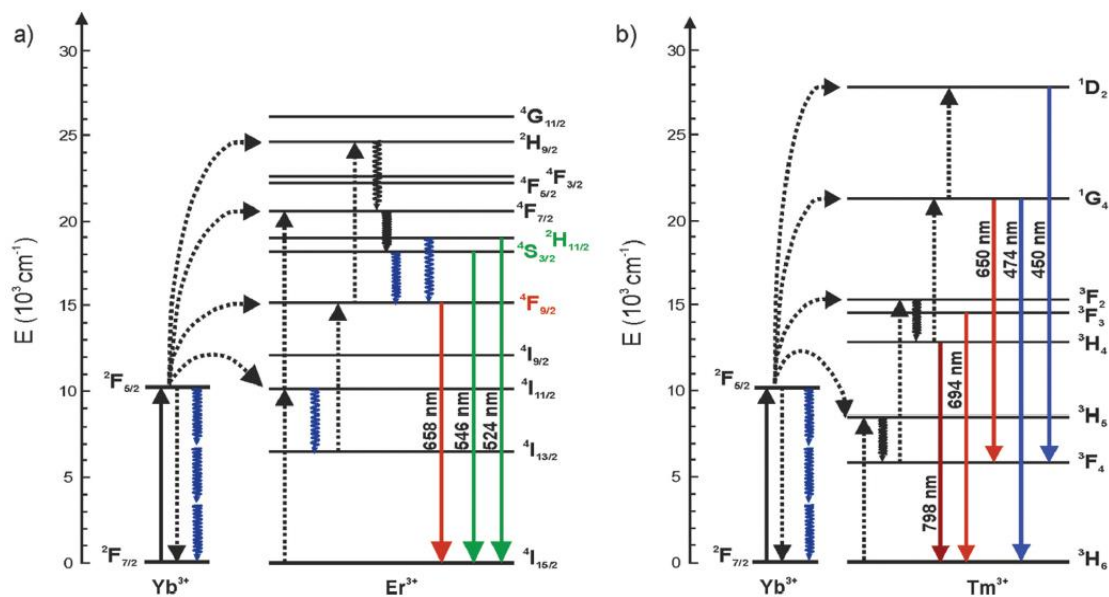


Figure 12. Energy level diagrams of (a) $\text{NaYF}_4:\text{Yb}^{3+},\text{Er}^{3+}$ and (b) $\text{NaYF}_4:\text{Yb}^{3+},\text{Tm}^{3+}$. Solid, dotted and wavy arrows represent photon absorption or emission, energy transfer and relaxation processes, respectively. The blue wavy arrows denote the increased multiphonon relaxations caused by OH vibrations.²⁷

1.8 Aim of the thesis

In the last years bismuth ferrite thin films have acquired much more interest thanks to the narrow optical band gap and corresponding response in visible light. Thus, among other perovskite-type semiconductors, BFO appears as a promising photoactive material for energy harvesting and photoelectrocatalysis.²⁸ It has been also demonstrated that the BFO conductivity type and photocatalytic properties strongly depend on the crystal structure and the morphology of the material.

Recent works reported the use of BFO material in the construction of photocatalytic-luminescent heterostructures in which the NIR light absorption is carried out by lanthanide-doped UCNPs, which are used as cores in the synthesis of a core@shell system.²⁹

In this thesis work, controlled and reproducible nanostructured bismuth ferrite thin films were prepared, with a more easily manageable arrangement for application into devices, comparing with the powdered material.

Also, UCNPs were dispersed in the BFO thin films during the preparation and the modifications of morphology as well as the properties were investigated. The final goal is to demonstrate the correlation between a more homogeneous nanostructured morphology and the increasing in photoelectrocatalytic performance of the material.

Furthermore, optical investigations were carried out to search for the presence of upconversion emission within the thin films and to prove the energy transfer between the UCNPs and BFO.

In particular, absorption band of BFO at around 500 nm overlaps with green emission of Er^{3+} and with blue emission of Tm^{3+} .

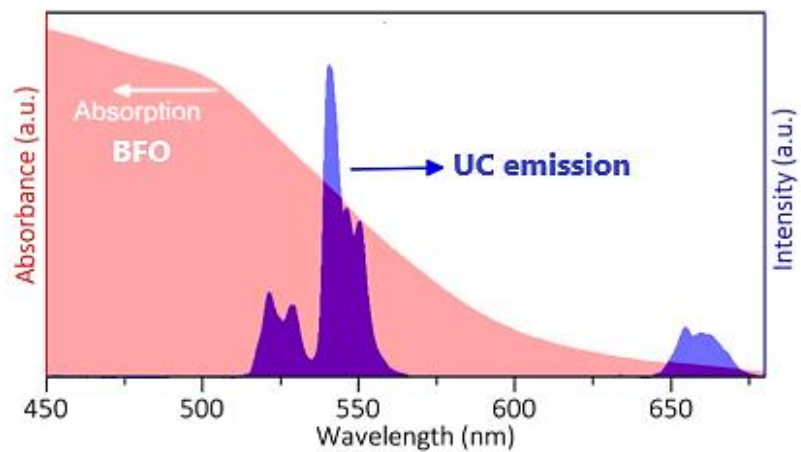


Figure 13. Schematic illustration of spectral overlap of the absorption of BFO (pink) and emission of the UCNPs (blue).

This experiment is a proof of concept of the possibility to extend the spectral range of absorption of BFO material also to the NIR portion of electromagnetic spectrum, thus exploiting the infrared portion of sunlight radiation.

2 CHARACTERIZATION TECHNIQUES

2.1 X-Ray Diffraction

XRD is a technique used to investigate the structure of a crystalline material, in which a beam of incident X-rays is diffracted into many specific directions. By measuring angles and intensities of diffracted X-rays, it is possible to calculate the structure of the crystals. Atoms in the crystal lattice scatter the X-rays because they have wavelength of the same order of magnitude as the spacing between lattice planes (1-100 Angstroms). The scattered waves produce mostly destructive interference and in few directions they sum up giving constructive interferences. The constructive interferences are determined by the Bragg's law

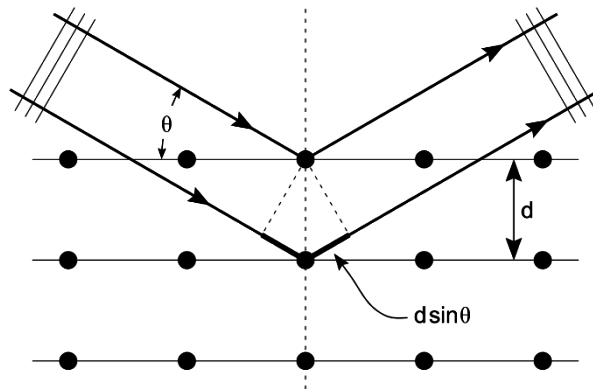


Figure 14. A two-dimensional crystal lattice and a set of imaginary planes is represented by the grid. X-rays incident on the crystal at an angle ϑ produce coherent diffraction when the difference in the travelled distance is equal to an integer multiple of the wavelength

$$2d \sin \theta = n\lambda$$

where d is the spacing between the diffracting planes, θ is the incident angle of the diffraction beam, n is an integer number and λ is the wavelength of the beam (see Figure 14).

The constructive interferences generate spots in the so-called diffraction pattern. The basic features of a diffraction experiment are (1) the generation of the X-rays beam through the collision of accelerated electrons from a hot cathode with the anode, usually Mo, Cu, Ag, (2) the diffraction by the lattice planes of the sample, (3) the detection of the diffracted beam with a scintillation counter and a pixel detector or a charge-coupled

devices (CCD), rotating the sample (or the detector) to collect all the information, (4) the identification of lattice planes through peak analysis.

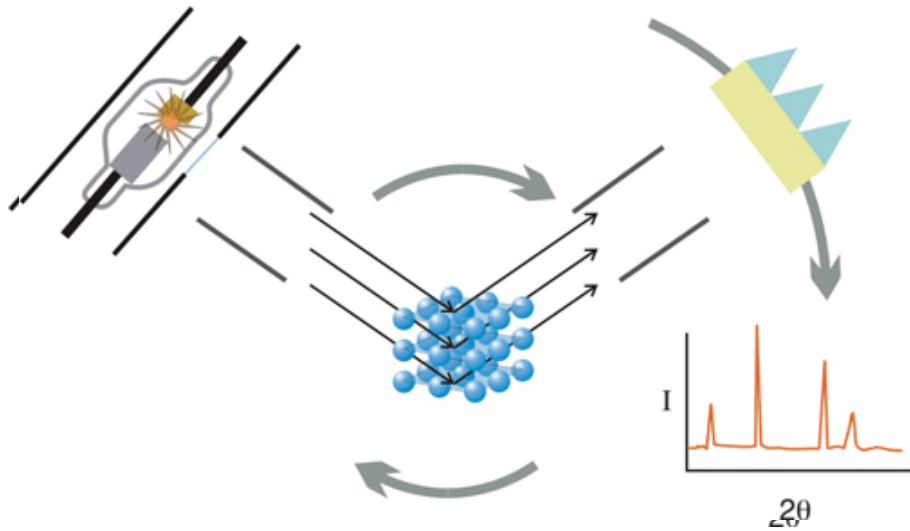


Figure 15. Scheme of the fundamental steps in a diffraction experiment.

Diffraction peaks give different information: their position in 2θ , as well as the peak intensity, is indicative of a particular phase and material, defining the lattice planes, which are identified by the Miller indexes, and also the shift in 2θ indicates a uniform lattice strain, the peak width is used to investigate the particle or grain size.

XRD can be used for measuring the spacing between layers of atoms, determining the orientation of a single crystal or grain, identifying the phase of a material.³⁰

2.2 Electron Microscopy

The optical microscope has a resolution limit $R = \frac{0.61\lambda}{NA}$, with NA defined as numeric aperture, depending on the wavelength of the visible light used to create the image and to the technological problems in the fabrication of lenses.

This limit is overpassed by the electron microscope: using electrons instead of photons, the wavelength is between 0.6 until 0.001 nm and can be further diminished, increasing the acceleration of electrons. In electron microscopes, the electron beam is delivered on the sample using magnetic fields to deviate it, instead of glass lenses, avoiding the defects

carried by solid lenses. Thus, the final resolution with this technique is limited only by the damage caused by electrons hitting the sample.

Electron microscopes can be based on transmission (TEM) or scanning (SEM) microscopy.

In the SEM a straight beam of electron scans point by point and create a final image of the sample. From the interaction between the incident electrons and the surface of the sample, different signals are emitted:

- Backscattered electrons, from elastic scattering, give information about the composition of the sample
- Secondary electrons, from inelastic scattering, are produced by the ionization of sample atoms on the surface, so they give information about morphology
- Auger electrons are produced by an ionization of the atom inside the sample and a subsequent energy transfer to a more external electron
- X-rays, generated from ionization of atoms, have characteristic wavelengths and they give data about the chemical composition
- Cathodoluminescence is the emission of photons.

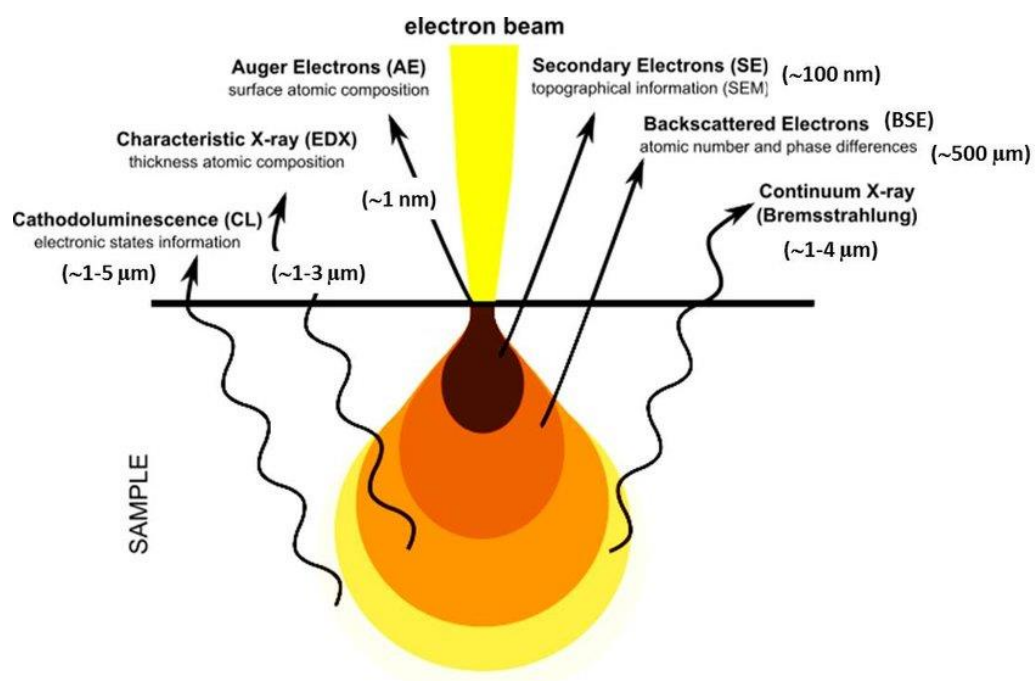


Figure 16. Image of the different signals that can be detected in the SEM analysis.

In order to obtain a tridimensional image of the surface of the sample, secondary electron must be analyzed. They are collected in a Faraday shield, a cage with an electropositive voltage, then they are converted into photons and amplified by a scintillator-photomultiplier system. The signal generates a current used to create an indirect image of the sample.

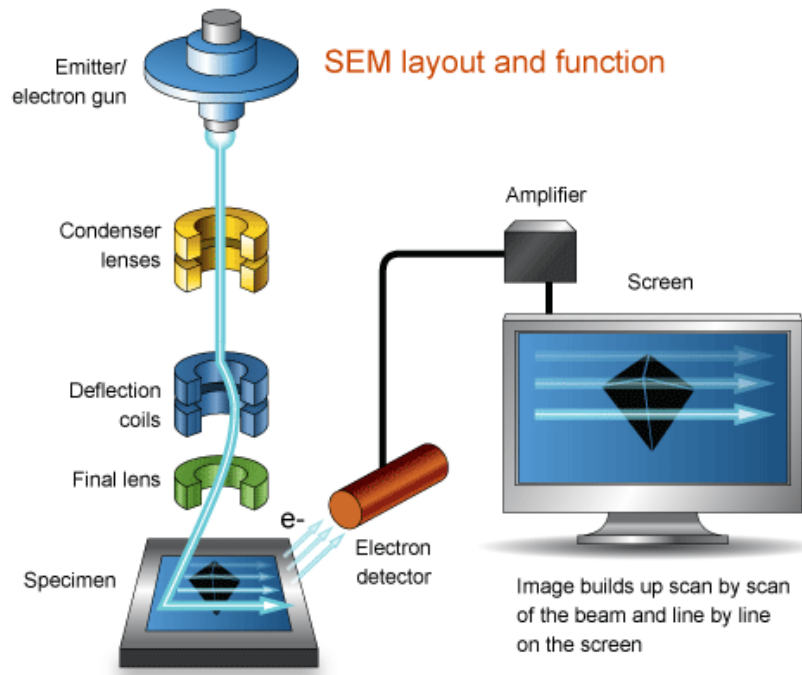


Figure 17. A general scheme of the scanning electron microscope and its principal components.

Different parameters can be modified to obtain a better image, for example acceleration voltage can be increased for a higher resolution, considering that this can damage the sample (in particular for biological one). In general, diminishing the working distance or reducing the spotsize (diameter of the electron beam) can also be useful to obtain a more resolved image of the sample.

Non-conductive samples must be prepared before the analysis, because they collect charge when scanned by the electron beam. The electron layer on the surface could cause image defaults and artefacts, so, in order to prevent the electrostatic charge, samples are coated by a thin layer of conductive materials, usually gold. This coating process is called sputtering and it is a deposition of an ionized plasma of metals, using electric or magnetic fields to confine the plasma atoms on the sample surface.

In the TEM the electrons, generated from the thermoionic source, are accelerated with the use of an ultra-high vacuum and high voltage, to generate an electron probe which is able to go through the sample. The sample must be thin enough ($\cong 100$ nm) to be crossed by the electrons. The image is formed because of the contrast between different regions of the sample, coming from differences in thickness or density, in atomic number, in crystal structure or orientation, energy loss by absorption of electrons from the sample.

Electron microscopy is able to give an extraordinary number of information with resolution at nanometric and atomic scale, thus SEM and TEM are regarded as fundamental tools in nanoscience and biological field.³¹

2.3 Spectroscopy

Spectroscopy concerns the investigation of interaction of light with matter. In spectroscopic techniques different types of electromagnetic radiation can be used, from UV light to microwaves, according to the entire spectrum of light, each one interacting in a specific way with matter. These investigations offer the possibility to acquire interesting information about composition, optical behavior, structure, electronic properties of materials and so on.

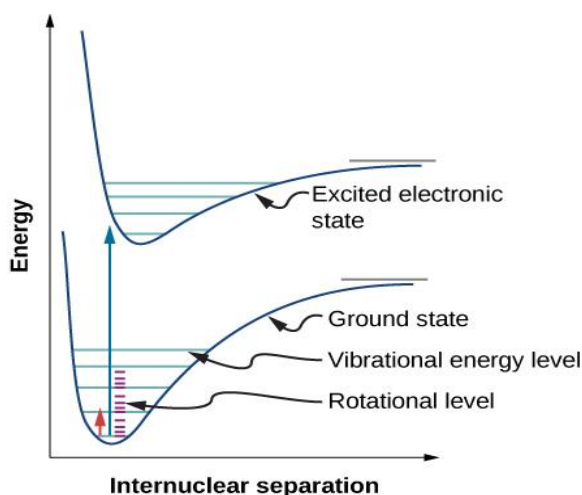


Figure 18. Energy states of a diatomic molecule. The curves represent the electronic energy levels; the lines marked are the vibrational levels inside each electronic level. Between two vibrational levels there are the rotational modes.

2.3.1 UV-Vis absorption spectroscopy and Tauc plot

In the UV-Vis spectroscopy, electronic transitions are involved, because the radiation has enough energy to permit an electron passage from one state to a higher energy one.

Absorption spectrum generally reports peaks which correspond to energy gaps, where specific radiation is absorbed by the sample, exciting an electron from the ground state to the first excited state.

A well-established method to determine the optical band gap of semiconductor starting from the absorption spectrum is the Tauc plot.³² It is based on the relation

$$(\alpha h\nu)^n = K(h\nu - E_g)$$

Where $h\nu$ is the incident photon energy, α is the absorption coefficient, K is an energy independent constant and E_g is the energy of the optical band gap. The exponent n depends on the nature of the transition, in particular $n=2$ for the direct band gap and $n=\frac{1}{2}$ for the indirect band gap. From the Tauc plot the energy gap can be determined from the slope and the abscissa intercept of a linear fit of the plotted data.

2.3.2 Laser spectroscopy

The upconversion emission is measured using a laser diode at 980 nm as excitation source. The laser is a solid-state semiconductor producing a coherent light beam in the infrared region and the emission from the excited sample is collected in the backscattering mode using the apparatus represented in the scheme below.

The setup includes the light source that is directed towards a dichroic mirror, which has very different transmission properties at different wavelengths. The beam at 980 nm is completely transmitted and an objective focuses it on the sample, that could be liquid as well as solid. The fluorescence coming back from the excited sample is almost totally reflected from the dichroic mirror and it is collected by an optical fiber, collocated after a 980 nm filter. A system of monochromator and CCD collects the signal separating the different wavelengths and translating collected photons into emission spectra.

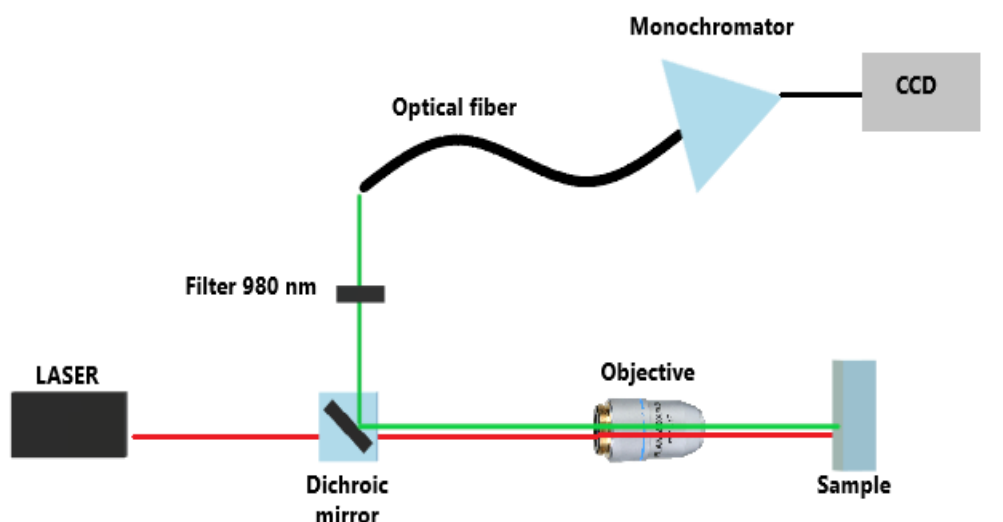


Figure 19. Scheme showing the setup for the emission experiment in backscattering mode.

2.4 PEC analysis

Photoelectrochemical (PEC) cells are actually solar cells based on the presence of a semiconductor-electrolyte interface. The investigation on the efficiency of the PEC cell is measured using the absorption of light or better the generated photocurrent from the photoelectrocatalyst. A commonly used method is the three-electrode measurement, based on a reference electrode which provides a reference potential, a working electrode linked to the photocatalyst material and a counter electrode, which ensures the correct functioning of the system.³³

The light source is provided by a solar simulator composed of a Xenon lamp and a power supply, giving the closest radiation to the natural one. The Xe lamp illuminates the electrolytic cell composed of the three electrodes immersed in an electrolytic solution such as sodium sulfate aqueous solution, essentially acting as an electrochemical conductor to allow current to flow through the solution. The electrolyte solution should be a good redox system, where protons should be the electron acceptors and water the hole acceptors.

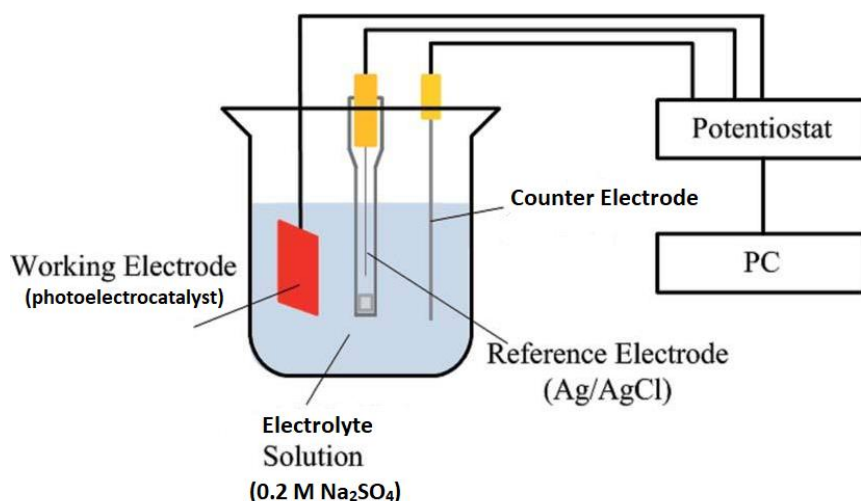


Figure 20. Schematic illustration of the three-electrode setup used to carry out photoelectrochemical analysis.

The electrodes are connected to the potentiostat, which is connected to the computer. A typical analysis is the Linear Sweep Voltammetry mode, which is used to measure the photocurrent at the working electrode while the potential E between the working and the reference electrode is swept linearly in time.

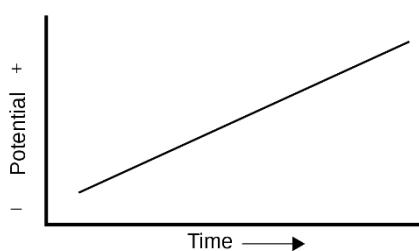


Figure 21. Linear potential sweep as a function of time.

When the delivered potential E approaches the reduction potential E_s of the molecule A in the electrolyte solution, the current on the surface of the working electrode increases and the flow of electrons in and out the electrodes causes the current. The generated photocurrent is a direct measure of the rate at which electrons are exchanged by the electrode/electrolyte system.

3 EXPERIMENTAL PART

3.1 Reagents

Bismuth (III) nitrate pentahydrate ($\text{Bi}(\text{NO}_3)_3 \cdot 5\text{H}_2\text{O}$, Sigma Aldrich), Iron (III) nitrate nonahydrate ($\text{Fe}(\text{NO}_3)_3 \cdot 9\text{H}_2\text{O}$, Alfa Aesar), 2-methoxyethanol ($\text{CH}_3\text{OCH}_2\text{CH}_2\text{OH}$, Sigma Aldrich), acetic anhydride ($(\text{CH}_3\text{CO})_2\text{O}$, Sigma Aldrich), sodium citrate tribasic dihydrate ($\text{HOC}(\text{COONa})(\text{CH}_2\text{COONa})_2 \cdot 2\text{H}_2\text{O}$, Sigma Aldrich), calcium chloride dihydrate ($\text{CaCl}_2 \cdot \text{H}_2\text{O}$, Sigma Aldrich), strontium chloride hexahydrate ($\text{SrCl}_2 \cdot 6\text{H}_2\text{O}$, Carlo Erba), ytterbium (III) chloride hexahydrate ($\text{YbCl}_3 \cdot 6\text{H}_2\text{O}$, Sigma Aldrich), erbium (III) chloride hexahydrate ($\text{ErCl}_3 \cdot 6\text{H}_2\text{O}$, Sigma Aldrich), thulium (III) chloride hexahydrate ($\text{TmCl}_3 \cdot 6\text{H}_2\text{O}$, Sigma Aldrich), ammonium fluoride (NH_4F , Baker), acetone ($\text{CH}_3\text{COOCH}_3$, Sigma Aldrich).

3.2 Synthesis of Bismuth Ferrite thin films

Bismuth ferrite (BFO) thin films have been synthesized with a previously reported sol-gel method.³⁴ The synthesis has been carried out varying the aging time of precursor solution, which has been prepared following the list of reagents reported in Table 1. Other parameters have been optimized during the synthesis, in order to obtain the optimal conditions for the synthesis of homogeneous pure material.

Reagent	Moles number	Volume/Grams	MW
$\text{Bi}(\text{NO}_3)_3 \cdot 5\text{H}_2\text{O}$	16.4 mmol	8 g	485 g/mol
$\text{Fe}(\text{NO}_3)_3 \cdot 9\text{H}_2\text{O}$	14.8 mmol	6 g	404 g/mol
2-methoxyethanol		20 ml	76 g/mol
Acetic anhydride		10 ml	102 g/mol

Table 1. Reagents used for the preparation of sol precursor of BFO.

BFO sol is prepared with the following procedure:

- The right amounts of bismuth nitrate pentahydrate and iron nitrate nonahydrate are mixed in 20 ml of 2-MOE
- The solution is stirred at room temperature for 30 minutes until the powders are completely dissolved
- Acetic anhydride (10 ml) is added to the solution and it is stirred for other 60 minutes



Figure 22. Bismuth ferrite precursor solution.

The as prepared precursor solution is stored under the fume cupboard and covered with parafilm and used for the thin film preparation at different aging times from day number 1 to day number 5.

Every day the same procedure for BFO thin film formation is followed:

- 2x2cm FTO glass squares are cut and subjected to washing procedure (5 minutes sonication in soap and water, 5 minutes sonication in acetone, 5 minutes sonication in 2-propanol)
- Before the coating, a tape is placed on the substrate to define the area that must be covered. One edge of FTO glass should be left uncovered during the BFO deposition to allow the PEC electrode connection
- The sol is deposited onto FTO substrates by spin-coating at 3000 rpm for 30 seconds



Figure 23. The G3P spincoat.

The material is subjected to a pre-annealing step where it is placed on a hot plate at 90°C for 1 minute and then on another hot plate at 350°C for 5 minutes. During these two steps the sol precursor undergoes gelation (at 90°C) and drying (350°C).

For the annealing step the sample is placed in a box furnace and the following steps occur:

- Ramp 1→ heating up to 450°C, heating rate of 5°C/min, dwell time 30 minutes: This step corresponds to pyrolysis.
- Ramp 2→ heating up to 650°C, heating rate 5°C/min, dwell time 1 hour. At this step there is the crystallization.

- Ramp 3 → cooling down to 25°C, cooling rate 5°C/min

The parameters that have been optimized during the synthesis are:

- Aging time of the precursor solution: precursor solution is deposited from day 1 to day 5, keeping the same conditions.
- Number of layers: thin films with 1, 3 or 5 layers have been prepared, performing the pre-annealing before each subsequent deposition and the annealing in the box furnace at the end.
- Annealing atmosphere: samples have been prepared changing the atmosphere inside the furnace, to perform the annealing step in air or in oxygen atmosphere.



Figure 24. BFO thin films (1 layer) deposited on FTO substrate, before the annealing step.

3.3 Synthesis of Upconverting Nanoparticles

Reagents	Moles (mmol)	Volume (ml)	Grams (g)
Sodium citrate			6.5
H ₂ O		21.5	
SrCl ₂	2.73	2.73	
YbCl ₃	0.752	0.75	
TmCl ₃	0.017	0.017	
NH ₄ F		2.5	

Table 2. Reagents used for preparation of SrF₂:Yb,Tm nanoparticles.

The upconverting nanoparticles SrF₂:Yb(21.5%),Tm(0.5%) have been synthesized with a well-assessed hydrothermal method.³⁵ The solution is prepared mixing the right amount of cation precursors (as 1M solutions) in a Teflon flask, with deionized water and sodium citrate. The solution is stirred until it becomes clear, then the ammonium fluoride solution is added and the flask is placed in autoclave for synthesis into the oven at 190°C for 3 hours.

After the heating step, the reaction is quenched, putting the autoclave in cool water, then nanoparticles are washed with acetone and they are collected with centrifugation at 8000 rpm for 10 minutes. The washing procedure is repeated two or three times and finally pellet of nanoparticles is stored under acetone.

The same procedure is used for the synthesis of CaF₂:Yb(20%),Er(2%) nanoparticles. The only difference is the amount of reagents added to precursor solution.

Reagents	Moles (mmol)	Volume (ml)	Grams (g)
Sodium citrate			6.5
H ₂ O		21.5	
CaCl ₂	2.73	2.73	
YbCl ₃	0.70	0.70	
ErCl ₃	0.07	0.07	
NH ₄ F		2.5	

Table 3. Reagents used for preparation of CaF₂:Yb,Er nanoparticles.

3.4 Synthesis of nanocomposite

For the synthesis of BFO thin films doped with upconverting nanoparticles, the precursor solution of bismuth ferrite has been prepared with the same procedure explained at point 3.1. Upconverting nanoparticles have been synthesized with the well-assessed hydrothermal method reported at point 3.2 and they are SrF₂ nanoparticles doped with 21.5% of Yb³⁺ and 0.5% of Tm³⁺ for emission in the blue region of the visible spectra and CaF₂ nanoparticles doped with 20% of Yb³⁺ and 2% of Er³⁺ for emission in the green portion of visible light.

The first attempt has been done dispersing 150 mg of SrF₂ nanoparticles in 9 ml of BFO precursor solution.

In a second try, different amounts of nanoparticles have been weighted, 50 mg, 100 mg and 250 mg have been mixed to BFO precursor solution.

To homogeneously disperse UCNPs in the BFO sol, nanoparticles have been first added to 1 ml of 2-MOE, sonicating for 1 hour until the solution appears clear. Then, solutions have been added to the respective amounts of BFO precursor solution at day 5 of aging time.

The precursor solution is stirred for few minutes and then deposition on FTO substrate is done using the spin coater. Samples undergo the steps of pre-annealing and annealing in the box furnace at temperatures previously explained.

The same procedure can be used to synthesize different nanocomposites, with other kinds of nanoparticles dispersed in the BFO matrix.

4 RESULTS AND DISCUSSION

4.1 Optimization of synthesis protocol of BFO

The first part of the thesis project has concerned the optimization of the protocol for the synthesis of BFO thin films in order to achieve the best performance for pure material and obtain a reproducible method for the synthesis.

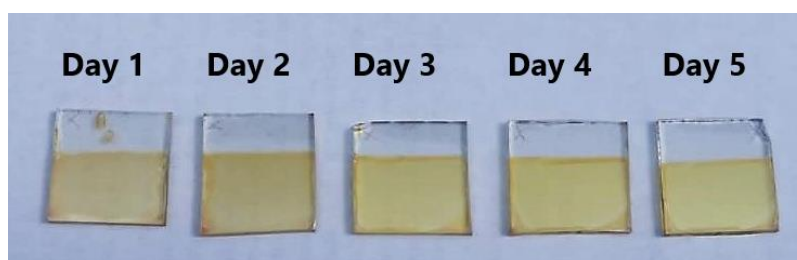


Figure 25. BFO samples deposited on FTO glass substrate from the same precursor solution at different aging times.

Since the synthesis is based on a sol-gel method and this process is influenced by the type of metal precursors, chelating agent, solvent and kinetic of reactions, aging time of the precursor solution is a key parameter for the hydrolysis and condensation processes to occur. Thus, the first step has been the synthesis of thin films (1 layer) using a precursor solution at different aging time (from day 1 to day 5). The solution has been prepared following the quantities and simple procedure explained in the experimental part and it was deposited at different days using the spin coater on FTO glass substrates. The pre-annealing and annealing conditions have been kept fixed.

Morphological characterization has been done using the Scanning Electron Microscope and the SEM images with same magnification have been compared for different samples. The morphology has been also correlated with the photoelectrocatalytic performance measured as Linear Sweep Voltammetry.

From this first experiment it has been observed that increasing the aging time the morphology was much more homogeneous and nanostructured and the number of holes in the thin film was decreasing. Furthermore, the increasing of PEC performance at day 4 and 5 could be related to the morphology of the material and could be reconducted to the conclusion that day 5 is the best day for the aging time.

SEM images for each day with the respective photocurrent curve measured applying a voltage have been reported below.

- **Day 1:** the morphology is poorly homogeneous, with a lot of big holes and nanoparticles of BFO that are polydispersed and this reflects the poor efficiency in photocurrent generation of the material.

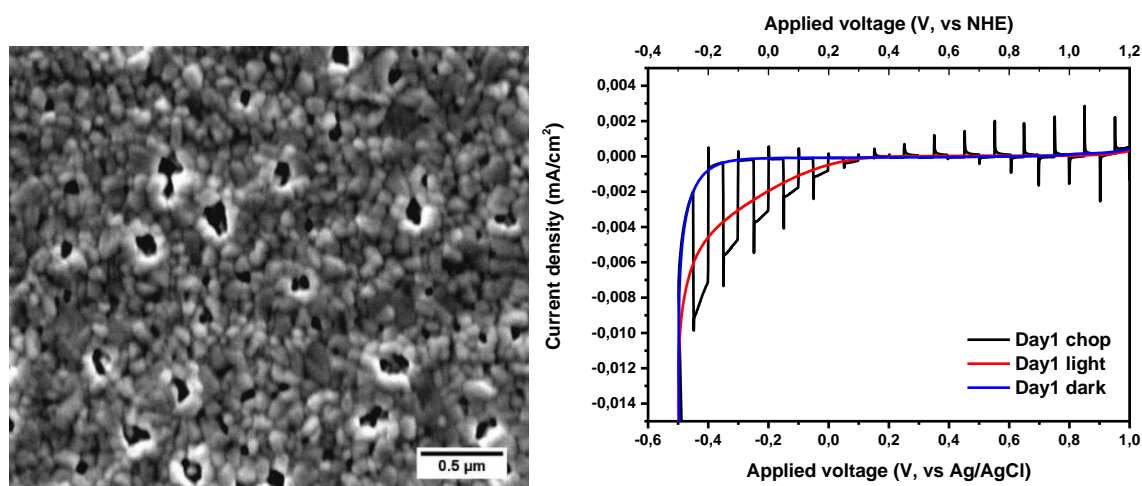


Figure 26. SEM image of BFO sample at day 1 (left) and respective current density acquired by performing Linear Sweep Voltammetry experiment (right).

- **Day 2:** as the previous sample, the morphology is inhomogeneous and the sample seems interacting with the electron beam of the SEM and this make difficult to acquire good images. The PEC performance is very low.

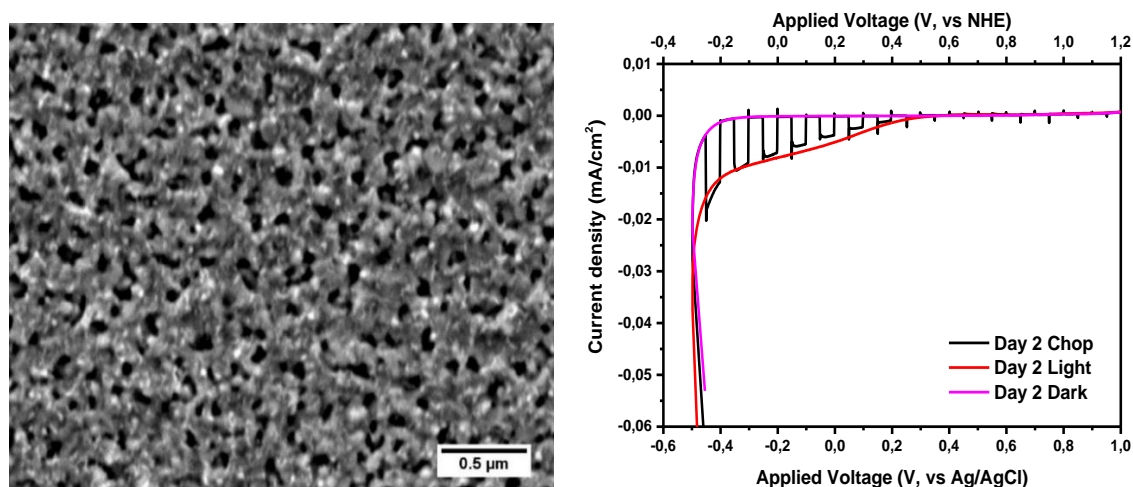


Figure 27. SEM image of BFO sample at day 2 (left) and respective current density acquired by performing Linear Sweep Voltammetry experiment (right).

- **Day 3:** this sample presents a more homogeneous morphology, with few holes and big crystals of around 200 nm together with smaller one. Despite the more regular aspect, the samples of day 3 still suffers from poor photoelectrocatalytic ability.

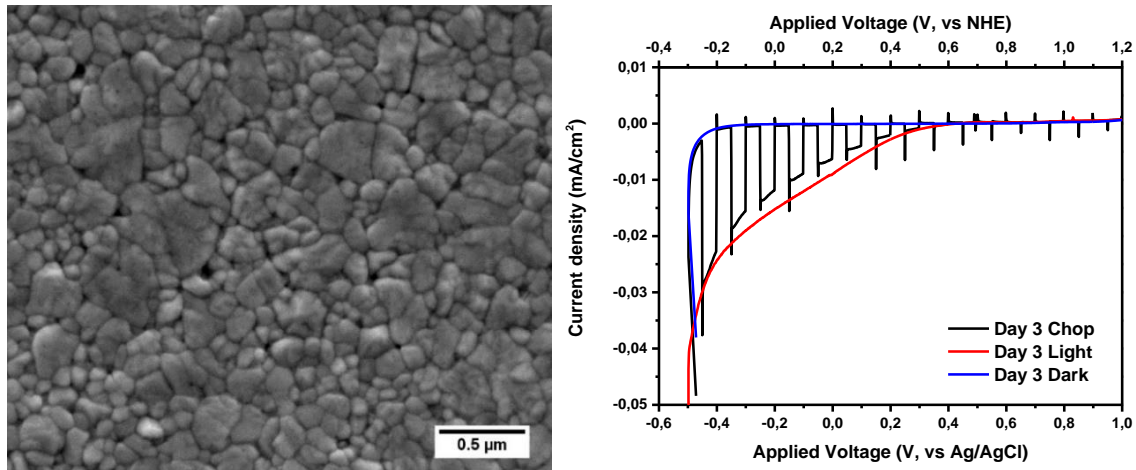


Figure 28. SEM image of BFO sample at day 3 (left) and respective current density acquired by performing Linear Sweep Voltammetry experiment (right).

- **Day 4:** the sample is homogeneous and there are a lot of small nanoparticles on the surface of the material, together with bigger ones. The increasing in the homogeneity is also reflected by the increasing in the PEC performance.

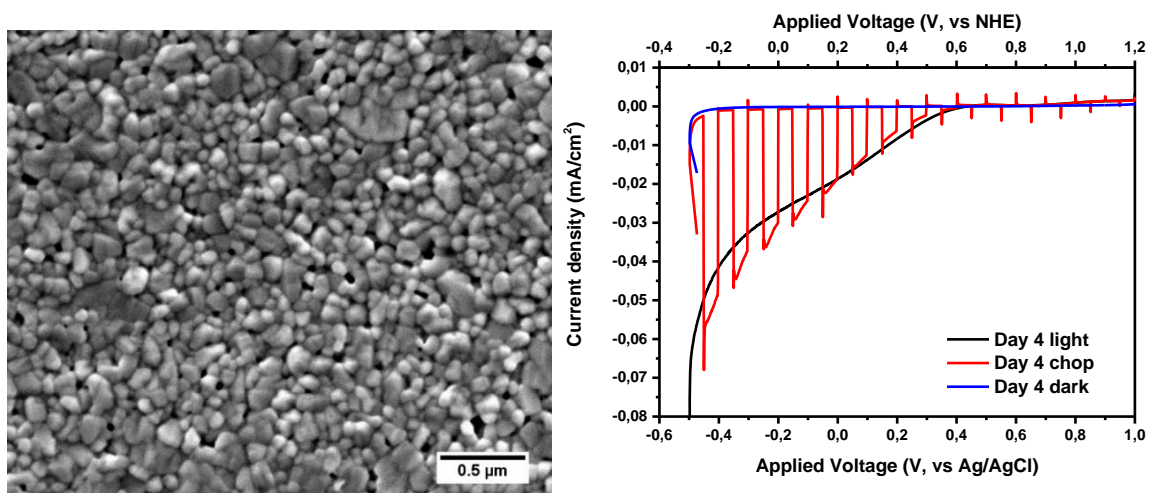


Figure 29. SEM image of BFO sample at day 4 (left) and respective current density acquired by performing Linear Sweep Voltammetry experiment (right).

- **Day 5:** surprisingly, the sample of day 5 appears much more similar to the day 3, with the same morphology, the same particle size and the same distribution of holes. Some roughening on the grains could be observed though, suggesting a higher surface area. In fact, this morphology shows high photocurrent generation, as in the case of day 4.

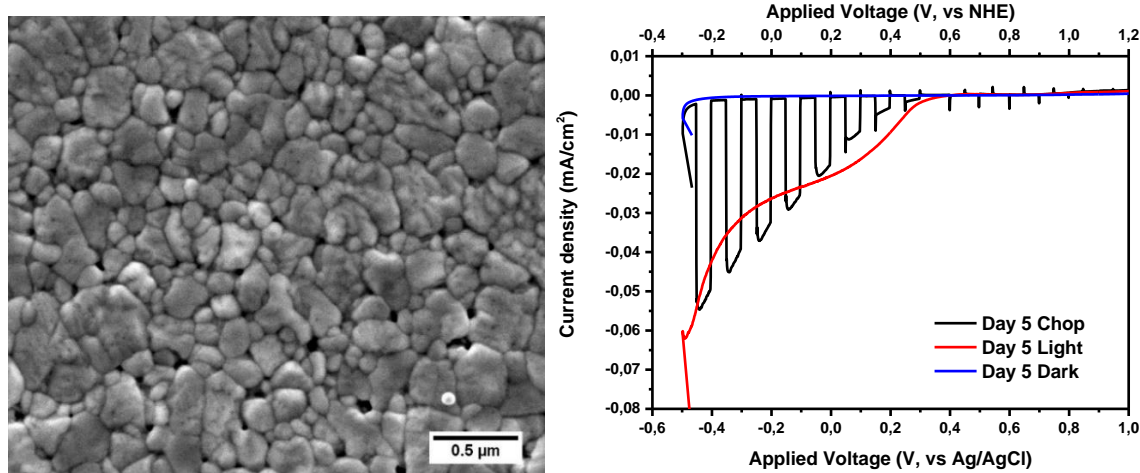


Figure 30. SEM image of BFO sample at day 5 (left) and respective current density acquired by performing Linear Sweep Voltammetry experiment (right).

As a conclusion of this first optimization part, it is possible to deduce that the best aging time for the precursor solution is 5 days, as shown from the PEC properties, where a photocurrent density of $-0.035 \text{ mA cm}^{-2}$ has been generated at 0 V versus NHE, illuminating with AM 1.5 simulated solar light.

In order to improve the photoelectrocatalytic performance, a strategy could be to increase number of layers, thus increasing the thickness of the sample. The procedure is exactly the same explained at point 3.1, but additional layers could be added using the spin coating, after the pre-annealing steps and before performing the annealing in the box furnace. The results for the samples of BFO deposited at day 5 of aging time, with 1, 3 and 5 layers have been reported in the following part. SEM images and PEC curves have been correlated and comparison has been done between the different samples.

- **1 layer:** BFO thin film with 1 layer appears homogeneous in the distribution of holes and particles, that measure about 100 nm and seem well defined. Holes are a greater number with respect to the previous sample (day 5, 1 layer) and this could be related to a changing in the volume of the reaction batch, and these holes could be the reason for the decreasing in the generated photocurrent.

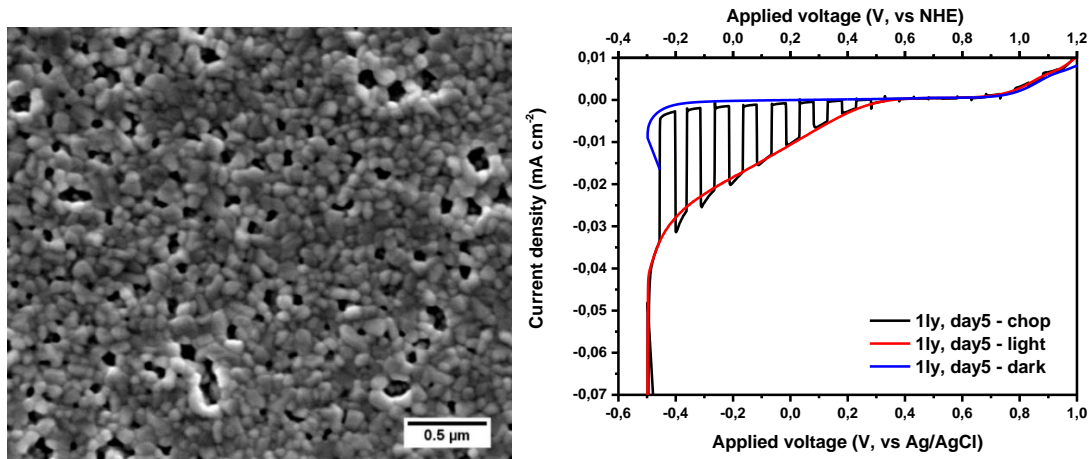


Figure 31. SEM image of BFO sample at day 5, 1 layer (left) and respective current density acquired by performing Linear Sweep Voltammetry experiment (right).

- **3 layers:** as expected, the morphology of the 3-layered sample is almost the same of the 1-layered, since they come from the same precursor solution. Surprisingly, the generated photocurrent is much lower than the previous sample and this could be due to the increasing in number of defects in the thin film structure or to the increasing in resistivity for the thicker film, which means higher recombination.

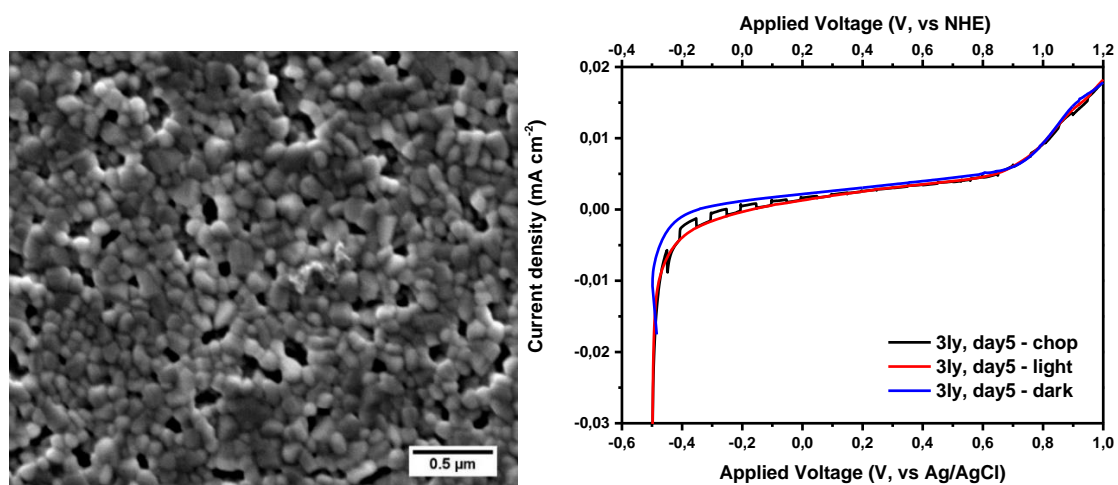


Figure 32. SEM image of BFO sample at day 5, 3 layers (left) and respective current density acquired by performing Linear Sweep Voltammetry experiment (right).

- **5 layers:** the same comparison could be done for the five-layered sample, that shows the same morphology of the previous one.

As it is possible to see from the curve for 5 layers sample, as well as the 3 layers, the photocurrent decreases dramatically increasing the number of layers. This is probably due to an increasing in the quantity of defects between one layer and the other and a less homogeneous sample.

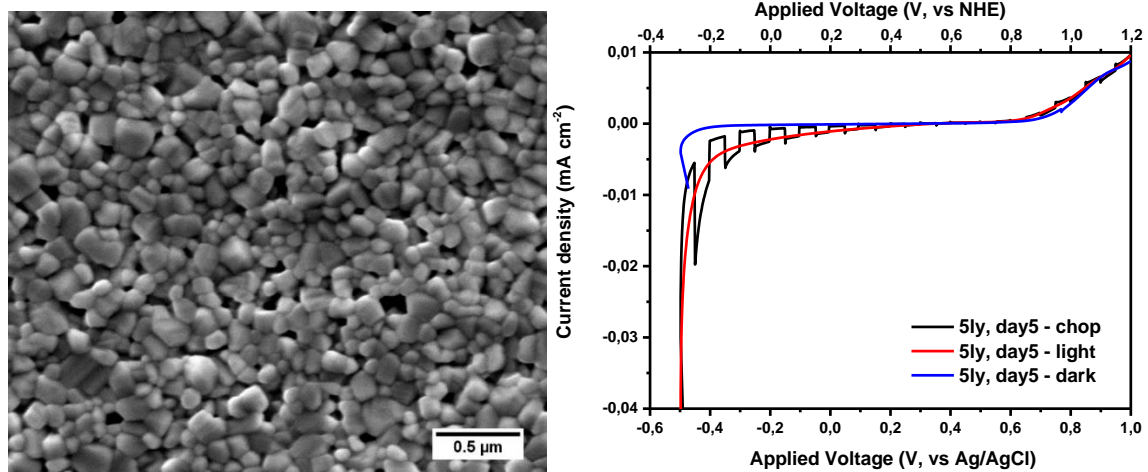


Figure 33. SEM image of BFO sample at day 5, 5 layers (left) and respective current density acquired by performing Linear Sweep Voltammetry experiment (right).

From these experiments it is possible to conclude that the best configuration for the material is the one-layered thin film deposited at day 5.

As last part of the synthesis optimization, the same procedure has been repeated, changing the annealing conditions and doing the annealing in oxygen atmosphere for the sample of 1 layer, day 5.

Changing the annealing conditions, as for example varying the growing atmosphere from reducing to oxidant, has been proved to change defects structure in the BFO, on which the p and n type conductivity depends. The annealing in oxygen atmosphere is expected to increase the p-type conductivity and so increase the photocurrent generation applying a negative voltage, as reported from Yilmaz et al.³⁴

SEM image of the sample obtained after annealing in oxygen atmosphere and the curve from PEC analysis have been displayed below. The morphology of the sample is almost

the same of the material obtained from annealing in air. Unexpectedly the generated photocurrent is not increased with respect to the previous sample

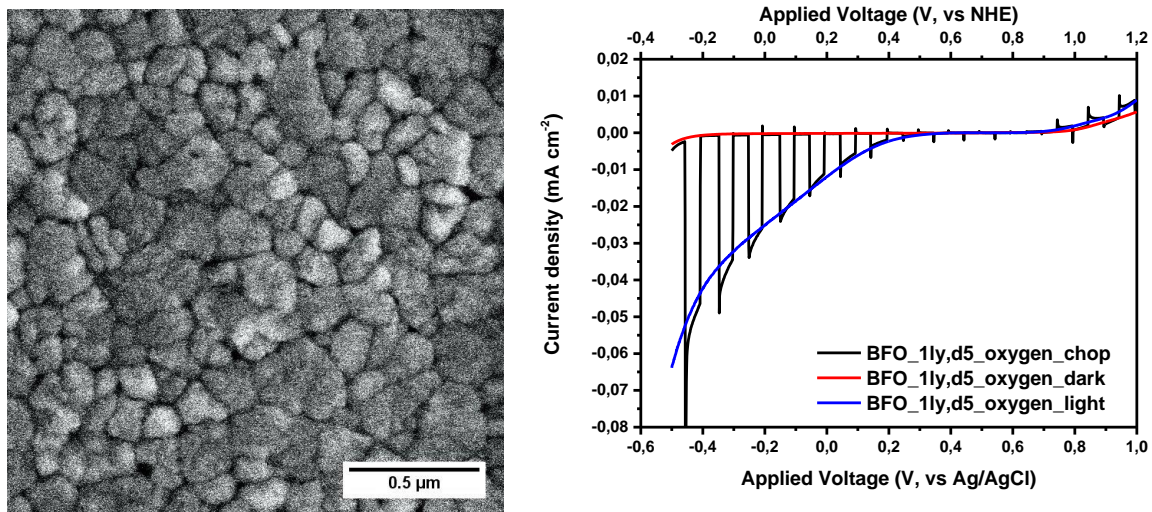


Figure 34. SEM image of BFO sample at day 5, 1 layer, oxygen atmosphere (left) and respective current density acquired by performing Linear Sweep Voltammetry experiment (right).

Since no improvement has been found in the morphology or in the photoelectrocatalytic properties, it seems reasonable to deduce that the best conditions for the BFO thin films synthesis are deposition at day 5, 1 layer and annealing in air. The graphs below show how the generated photocurrent changes with increasing of aging of precursor solution.

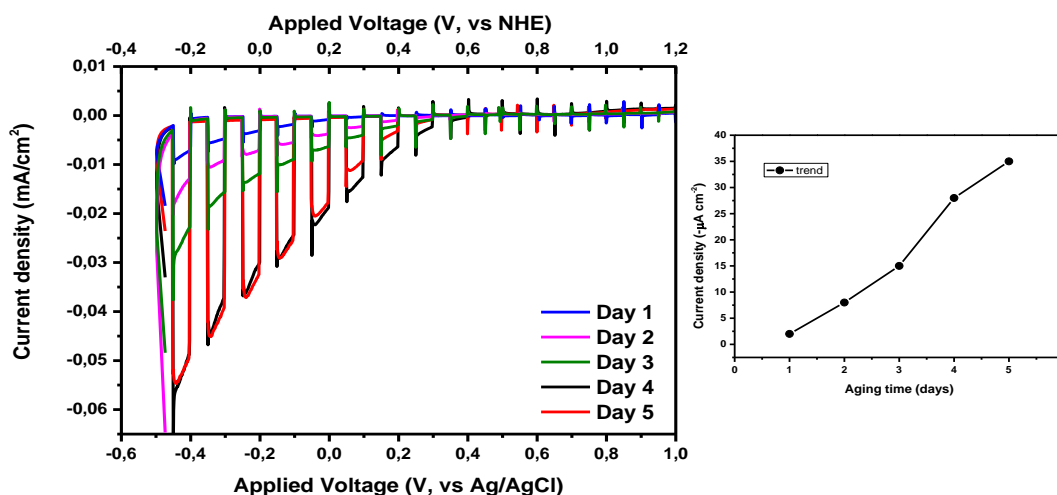


Figure 35. The chop curves for samples at different aging times are compared in the left image. The current density at 0 V vs. NHE is plotted against the aging time of the precursor solution to show the increasing in performance (right).

UV-Vis absorption spectroscopy has been used to investigate the optical properties of the samples. The measurements have been done using the Lambda 950 UV/VIS spectrometer by PerkinElmer, using a detector with integrating sphere for the analysis of thin films. The spectra have been acquired with the absorbance mode and the blank has been done with the FTO glass alone to remove its absorbance. The direct band gap calculations have been done using the Tauc method, where the Tauc and Davis-Mott relation has been used to probe the optical band gap of the thin film from the UV-VIS absorption data.

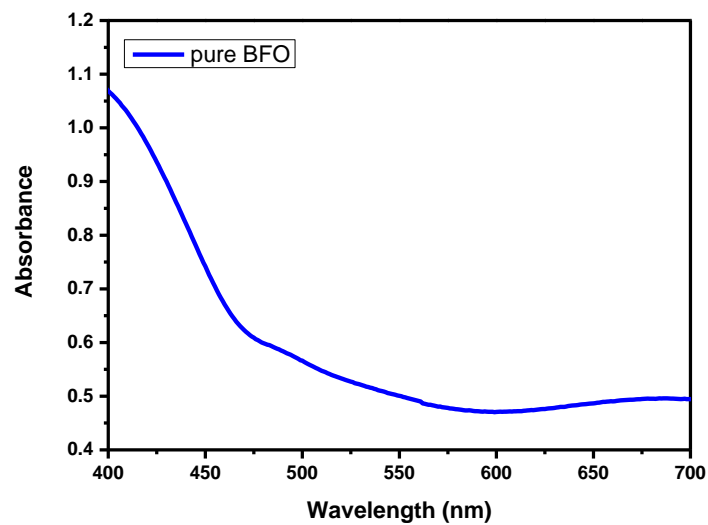


Figure 36. UV-Vis absorption spectrum of BFO thin film synthesized at day 5, 1 layer, in air atmosphere.

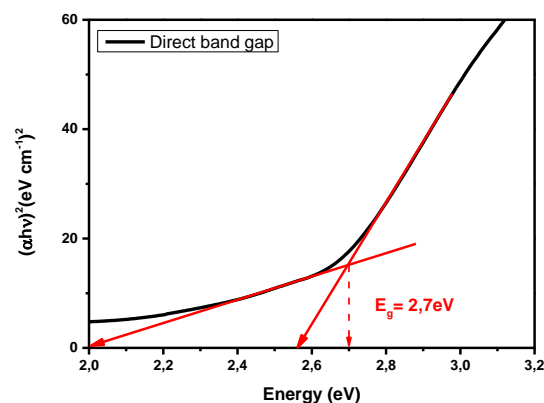


Figure 37. Tauc plot showing the direct band gap of the BFO thin film.

The significant absorption of BFO thin films in the visible range of radiation has been shown in the absorption spectrum (Fig. 38), starting at around 550 nm for pure BFO and increasing as the wavelength approaches the UV region. The absorption at longer

wavelengths with respect to other semiconductors and TiO_2 can be attributed to the narrow band gap. In particular, BFO possesses a direct band gap that has been found to be in good agreement with the one in literature, between 2.0 and 2.8 eV.

Raman spectrum of the BFO sample have been acquired using the Renishaw Raman microscope and 785 nm laser excitation, with a laser power of 10 mW.

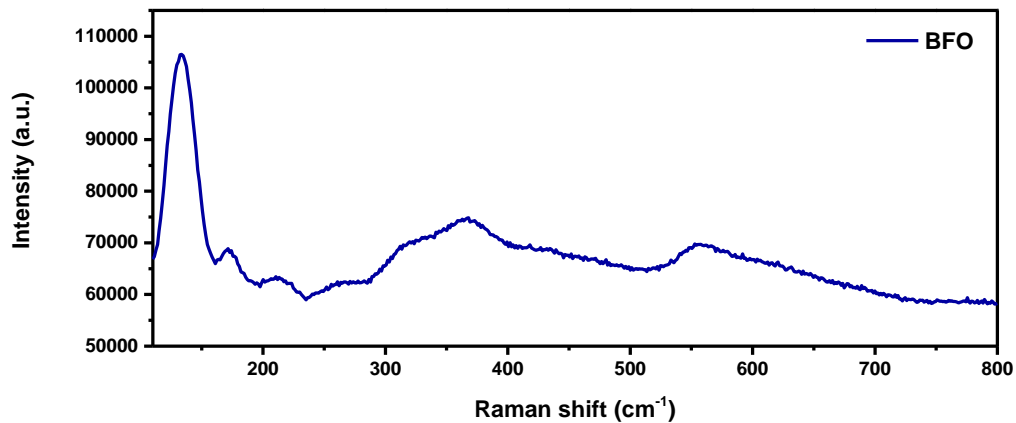


Figure 38. Raman spectrum of BFO thin film.

There is a lot of autofluorescence in the spectrum because it is a thin sample of 1 layer only, so the FTO signal is high but it is still possible to compare the spectrum with the ones found in literature^{36,37} and see that they are very similar, with the same peaks in the region between 100 and 250 cm^{-1} .

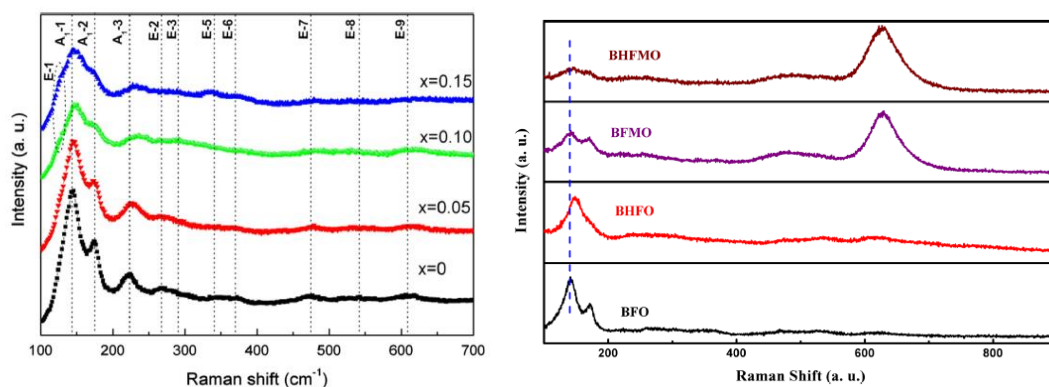


Figure 39. Raman spectra of BFO taken from literature, showing similar peaks to the experimental ones in the region between 100 and 250 cm^{-1} .

X-Ray diffraction spectroscopy has been carried out on the sample of pure BFO to investigate the crystalline structure of the material. It corresponds to the rhombohedral

perovskite-type structure belonging to the $Rc3$ space group. The BFO XRD pattern is also compared with the FTO glass diffraction pattern, in order to evidence the lines coming from the substrate. The characteristic crystallographic planes of BFO are shown, named with the Miller indexes (hkl).

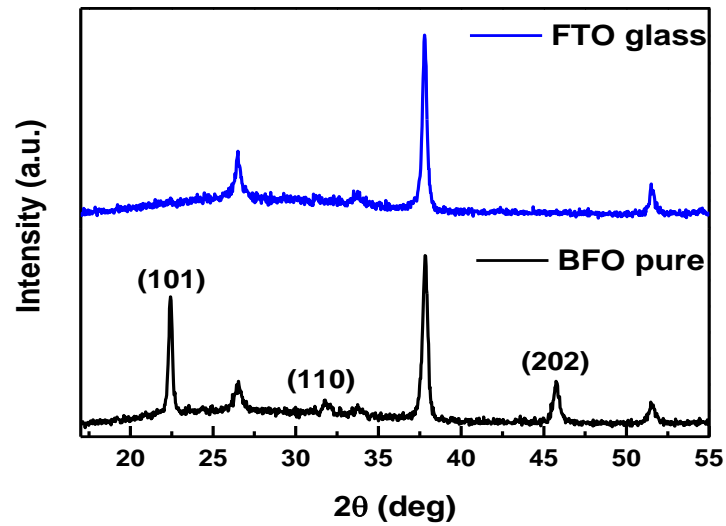


Figure 40. X-ray diffraction pattern of FTO glass substrate (blue) and pure BFO deposited on the glass substrate (black).

4.2 Characterization of Upconverting Nanoparticles

Upconverting Nanoparticles co-doped with Yb^{3+} and Er^{3+} or with Yb^{3+} and Tm^{3+} have been previously synthesized following the simple protocol at paragraph 3.3 and then characterized using X-Rays diffraction technique, TEM and laser spectroscopy under 980 nm excitation.

TEM images of the samples show nanoparticles with spherical morphology and size in the range 8-10 nm. Nanoparticles appear quite monodispersed and not aggregated, so they are promising candidates for their dispersion in other systems.

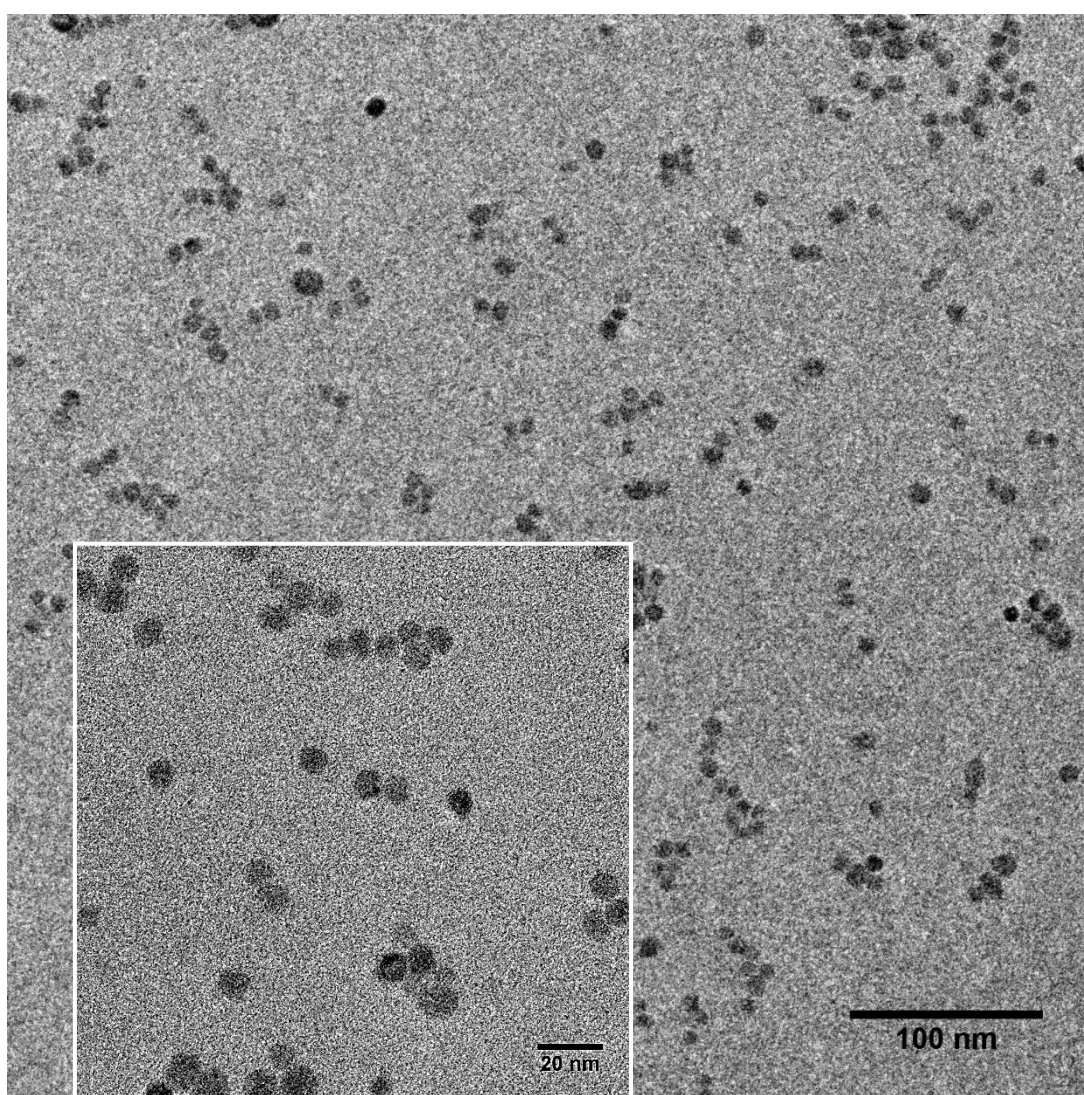


Figure 41. TEM images of CaF_2 nanoparticles showing spherical morphology and good monodispersity.

XRD analysis and Rietveld refinement on upconverting nanoparticles has been carried out. Both SrF_2 and CaF_2 crystalline structure match with the respective database patterns, as shown in Figures 42-43. The XRD patterns confirm the cubic crystal phase of the two nanomaterials and an average size around 10 nm, in agreement with the TEM images.

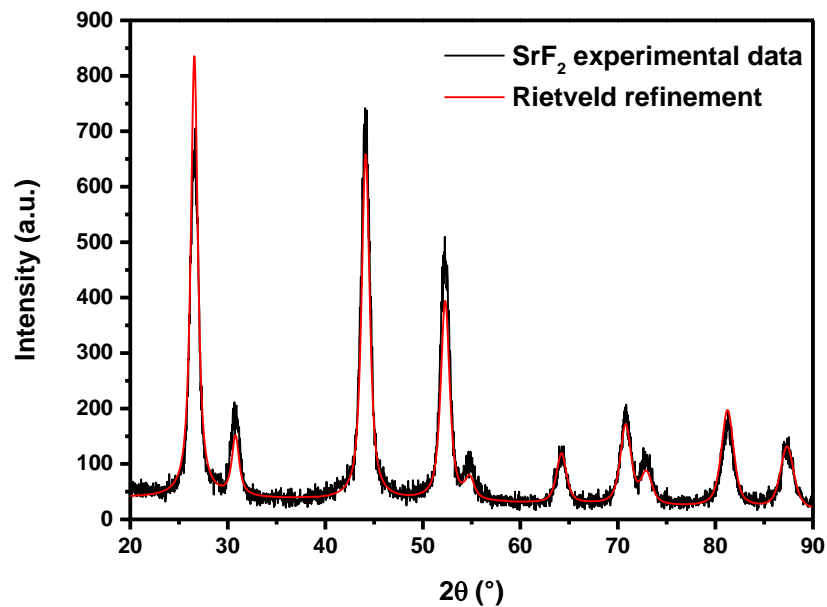


Figure 42. X-rays diffraction pattern of SrF_2 :Yb,Tm NPs

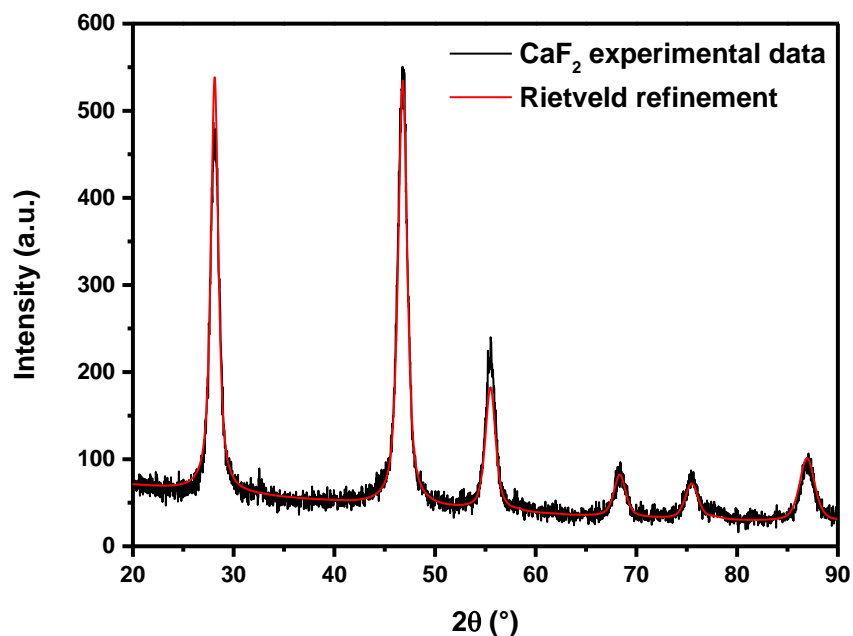


Figure 43. X-rays diffraction pattern of CaF_2 :Yb,Er NPs.

Emission spectra of UCNPs have been recorded from a solution in deionized water with a concentration of 25mg/ml using a laser excitation at 980 nm. In both samples the sensitizer is the Yb^{3+} which is excited from 980 nm laser radiation causing the transition $^2\text{F}_{7/2} \rightarrow ^2\text{F}_{5/2}$.

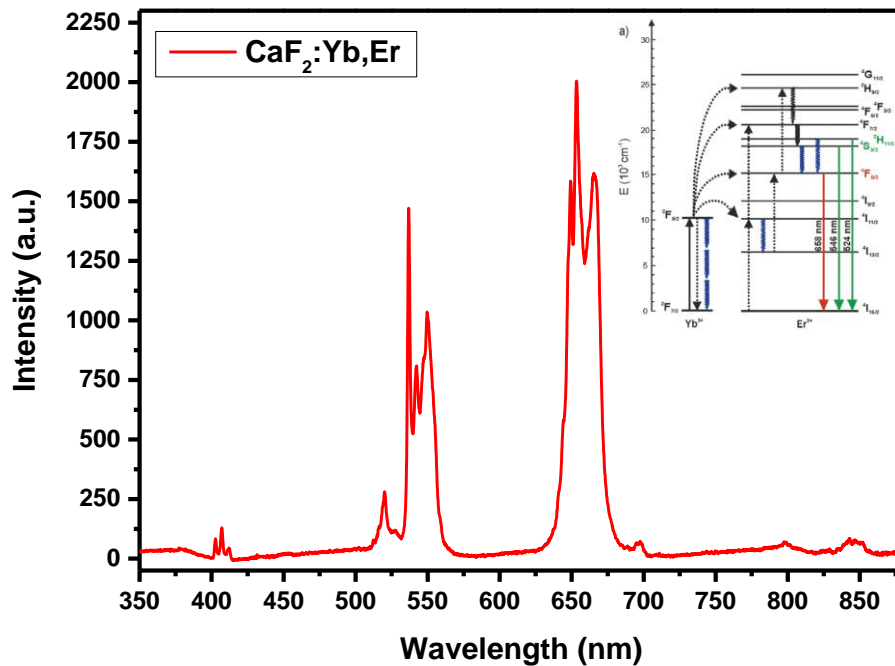


Figure 44. Upconversion emission spectrum of NPs: Yb^{3+} , Er^{3+} under 980 nm laser irradiation. The inset on the upper right shows the energy level diagram for the energy transfer.

The spectrum in Figure 44 shows the typical upconversion emission of Er^{3+} which acts as activator and it is excited by Yb^{3+} through an energy transfer mechanism (see inset). The green emission at 524 nm and 546 nm are attributed to $^2\text{H}_{11/2} \rightarrow ^4\text{I}_{15/2}$ and $^4\text{S}_{3/2} \rightarrow ^4\text{I}_{15/2}$ transition, respectively, while the red emission at 658 nm is attributed to the $^4\text{F}_{9/2} \rightarrow ^4\text{I}_{15/2}$ one.

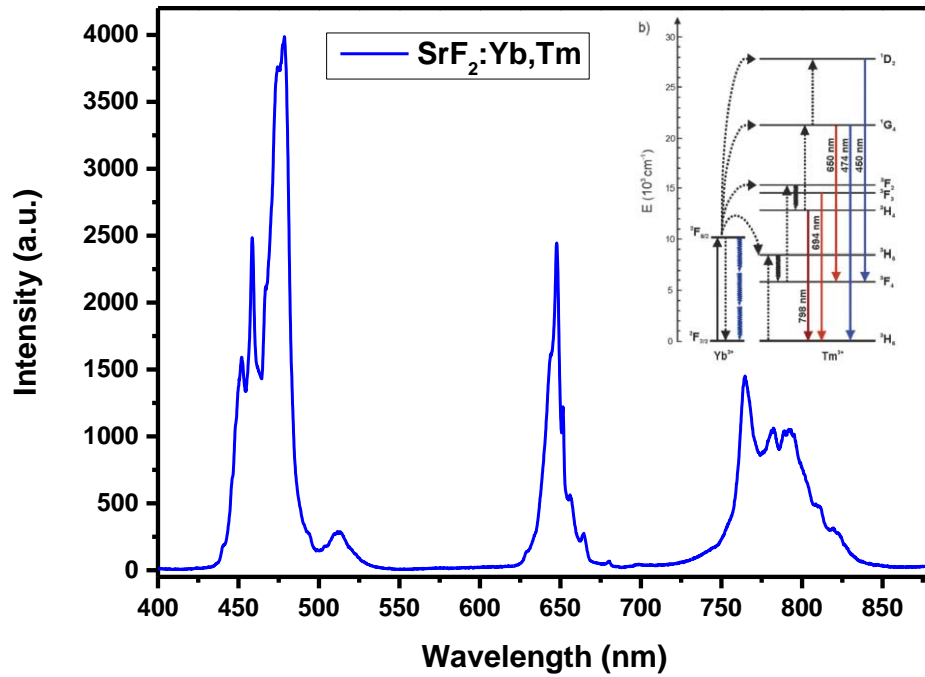


Figure 45. Upconversion emission spectrum of NPs: Yb^{3+} , Tm^{3+} under 980 nm laser irradiation.

Figure 45 shows the upconversion spectrum of $\text{SrF}_2:\text{Yb}^{3+},\text{Tm}^{3+}$. The $^1\text{D}_2 \rightarrow ^3\text{F}_4$ transition corresponds to emission at 453 nm, $^1\text{G}_4 \rightarrow ^3\text{H}_6$ transition to emission at 480 nm, $^1\text{G}_4 \rightarrow ^3\text{F}_4$ transition to emission at 650 nm, $^1\text{G}_4 \rightarrow ^3\text{H}_5$ transition to 770 nm emission and $^3\text{H}_4 \rightarrow ^3\text{H}_6$ one to emission at 800 nm.

4.3 Characterization of BFO-UCNPs nanocomposite

The first attempt of synthesis of nanocomposite has been done using previously prepared UCNPs of SrF₂: Yb, Tm, presenting UC emission in the blue and red of visible spectrum.

The nanocomposite has been deposited at day 1 and at day 5 of aging of BFO precursor solution, adding freshly prepared UCNPs solution in 2-MOE before the spin coating. Pure BFO samples have been also prepared with the same conditions to have a control during the characterization.

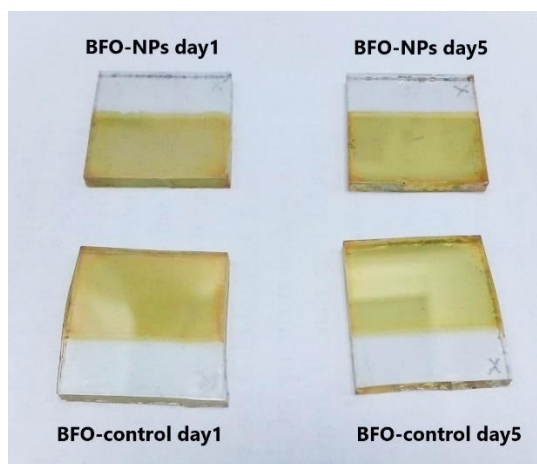


Figure 46. Image showing the nanocomposites prepared at different days, with the respective BFO control.

Linear Sweep Voltammetry analyses have been done to measure the curve of generated current versus applied voltage, normalizing the data for the illuminated area.

SEM images of the samples have been acquired and they have been reported below, correlating the morphology with the generated photocurrent.

As expected, the generated photocurrent of pure BFO deposited at day 1 is very low, confirming the previous experiments.

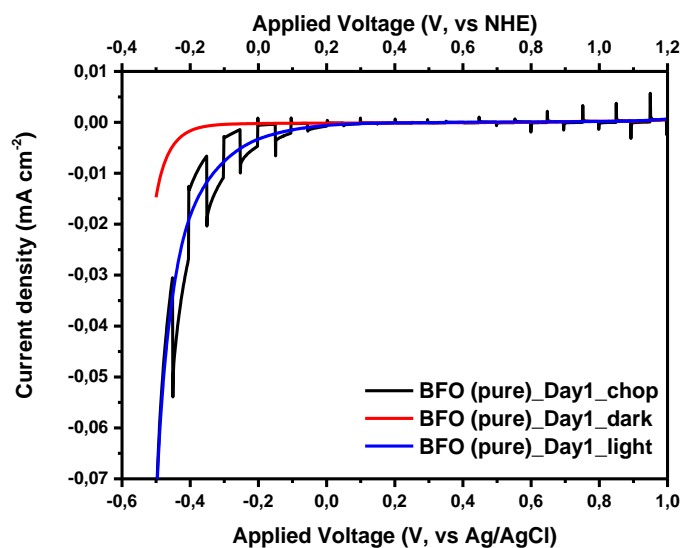


Figure 47. Linear Sweep Voltammetry experiment on pure BFO sample deposited at day 1 of aging of precursor solution.

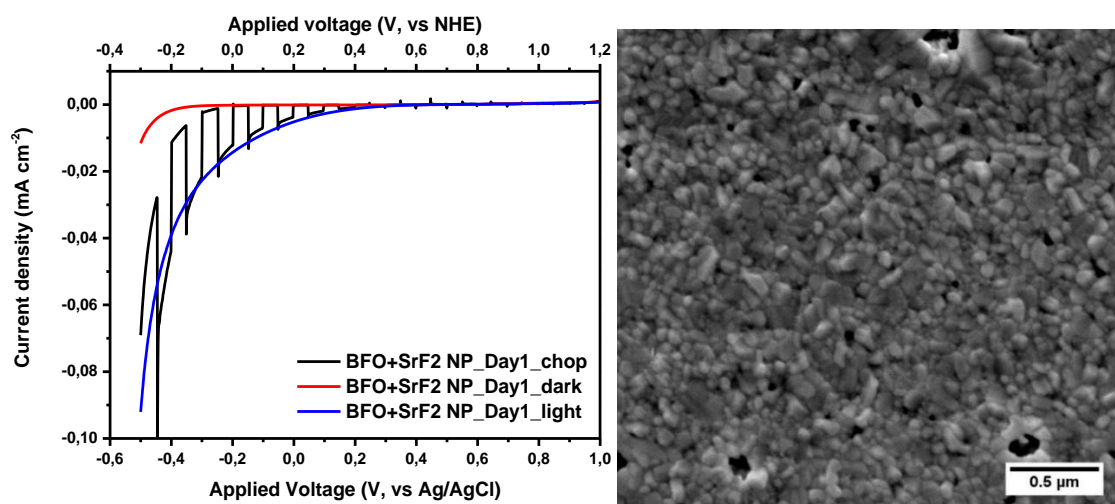


Figure 48. Generated photocurrent (left) and SEM image (right) for the sample of nanocomposite BFO+UCNPs prepared at day 1.

The morphology of nanocomposite prepared at day 1 is not perfectly homogeneous, even though the material is nanostructured, but there are not well distributed holes and this could affect the PEC performance.

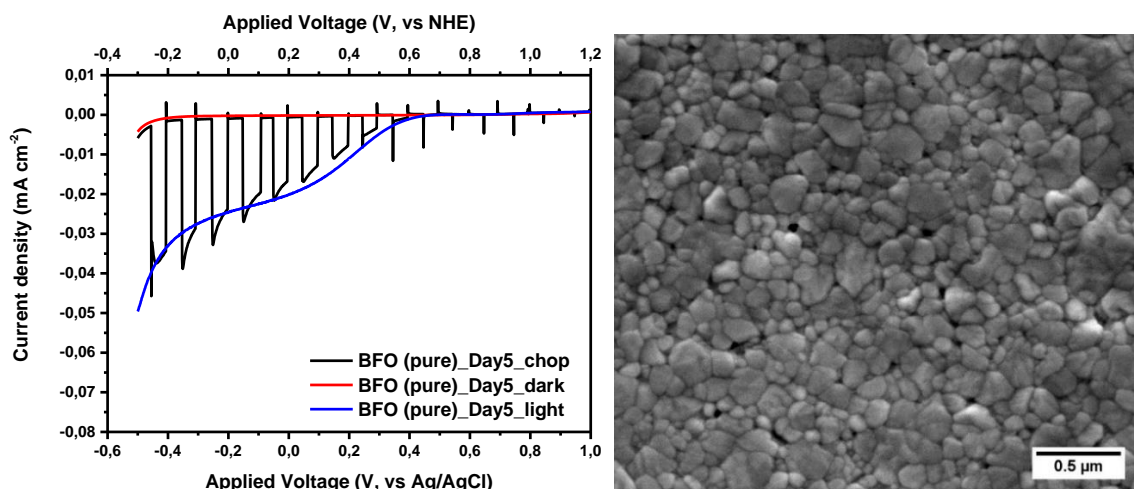


Figure 49. Generated photocurrent (left) and SEM image (right) for the sample of pure BFO prepared at day 5.

As a control of the reproducibility of the material, the pure BFO thin film day 5 has been analyzed too. The pure BFO at day 5 has exactly the same morphology of the previously synthesized (see paragraph 4.1), as well as the PEC properties. This demonstrates the benefit of the optimized method and the reproducibility of this sol-gel synthesis.

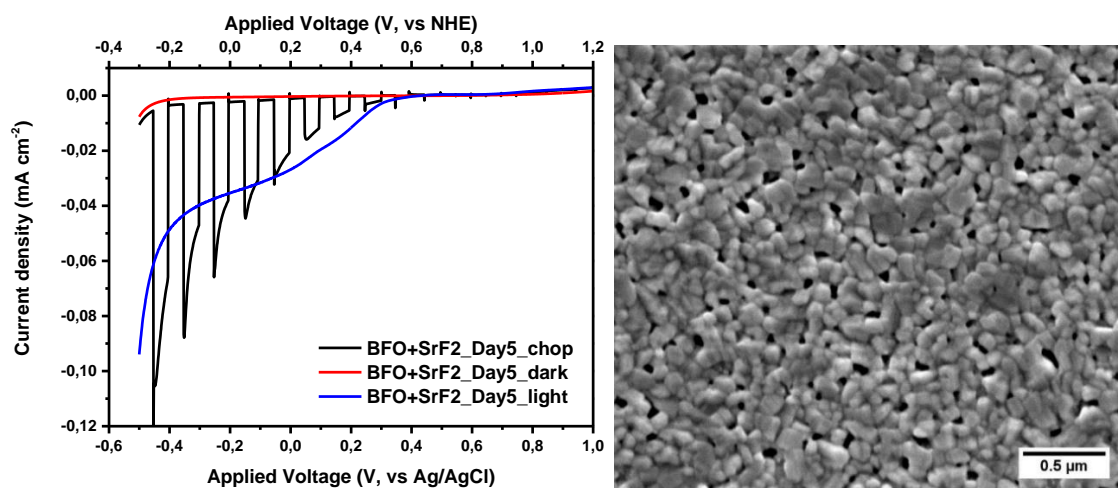


Figure 50. Generated photocurrent (left) and SEM image (right) for the sample of nanocomposite BFO+UCNPs prepared at day 5.

The BFO-NPs sample at day 5 presents a highly homogeneous morphology, with nanoparticles that seem stacked together, but they are very regular and measure around

100 nm and there is a good proportion between particles and holes, as expected from the high generated photocurrent.

As it is possible to deduce from the curves and according to the previous experiments, increasing the aging time of the precursor solution, the photocurrent increases dramatically of more than the 50%. Interestingly, the nanocomposite material with BFO and UCNPs shows a higher photoresponse with respect to the pure BFO, with an increasing in photocurrent of about the 35%, and the sample of BFO+NPs day 5 has the best performance ever found.

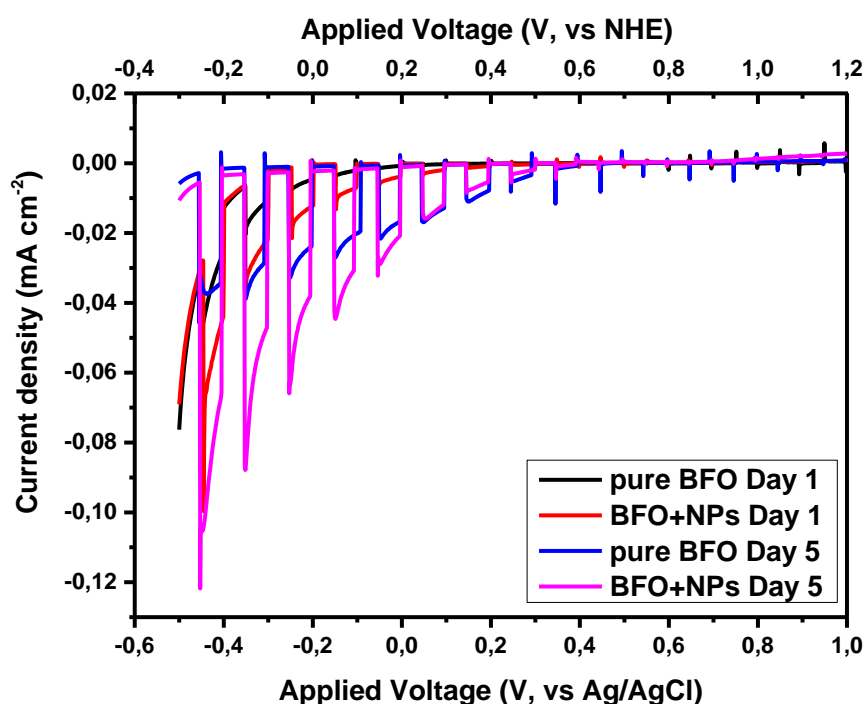


Figure 51. Overlapped curves of pure BFO samples and nanocomposite, showing the increasing in PEC performance.

The absorption spectrum of the nanocomposite deposited at day 5 have been acquired in the visible region of interest and the direct band gap calculations have been done using the Tauc plot method.

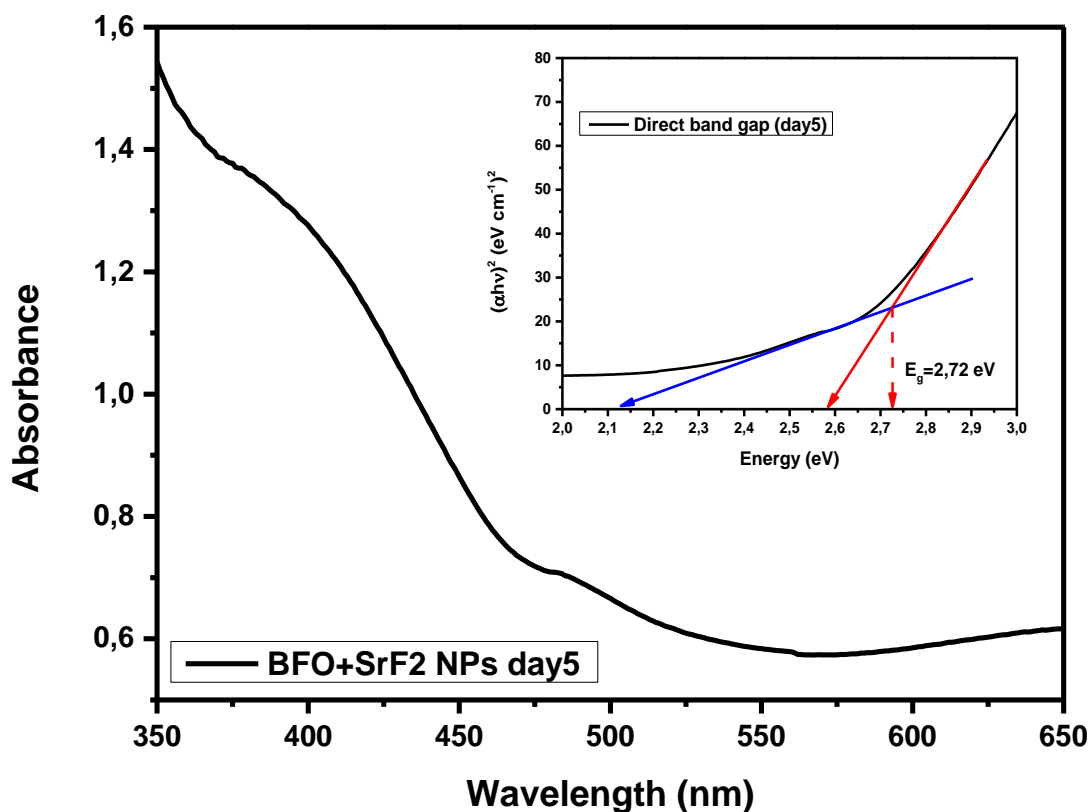


Figure 52. UV-Vis absorption spectrum of nanocomposite. The insets show the Tauc plot for direct band gap.

As reported in Figure 52, no significant difference has been found with respect to the pure material, showing the same band gap ($E_g = 2.7$ eV).

Subsequently, the nanocomposite has been synthesized using a higher concentration of $\text{CaF}_2:\text{Yb,Er}$ UCNPs, since no luminescence has been found from the previous samples irradiating the sample with laser at 980 nm and collecting the luminescence in the backscattering mode.

XRD pattern of nanocomposite sample is shown in Figure 53, with the FTO glass pattern as a comparison.

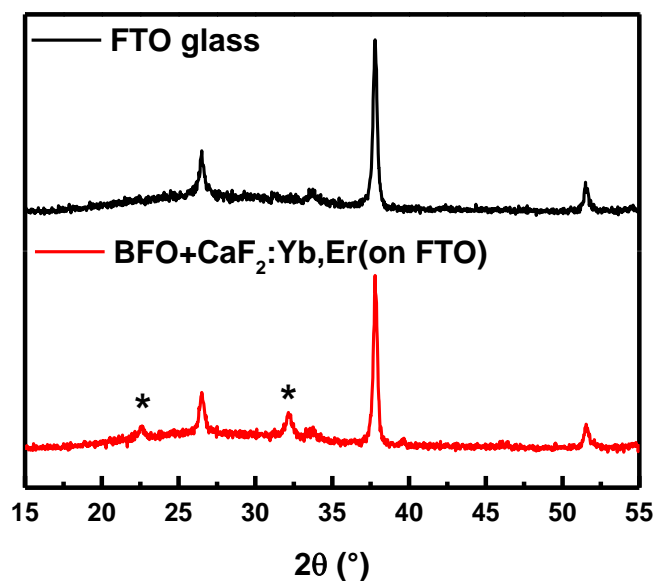


Figure 53. XRD pattern of nanocomposite (red) of BFO thin film with calcium fluoride UCNPs and of FTO glass substrate as a control (black).

The XRD pattern of BFO nanocomposite has very low signal-to-noise ratio and no peaks from the CaF_2 nanoparticles are observed, as they are very low in concentration. Probably the crystalline structure of BiFeO_3 has been strongly distorted by the addition of nanoparticles.

The presence of upconversion emission from the lanthanide-doped nanoparticles dispersed in the nanocomposite has been investigated using the Confocal-Multiphoton Leica TCS SP5 AOBs laser scanning microscope. This technique allows to excite the sample with a pulsed laser radiation in the infrared range, irradiating the sample point by point and to collect the emission in the visible range from each point with a system of prisms and a CCD camera. The samples have been excited with a 980 nm radiation and the images are recorded with a resolution of 8 BitsPerPixel and 80 nm/pixel.

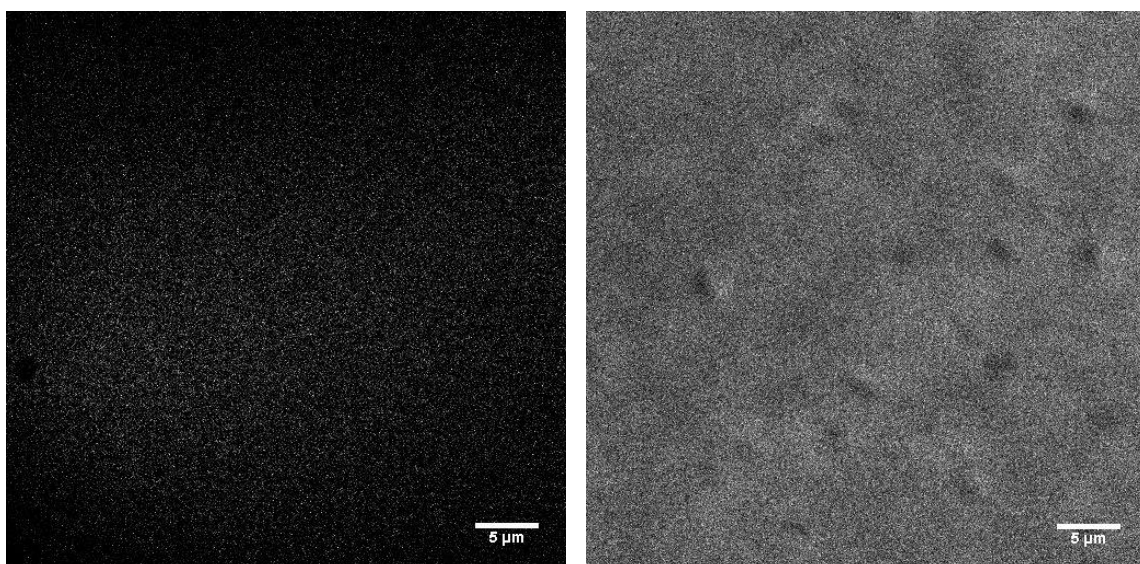


Figure 54. Multiphoton Laser Scanning Microscope images of pure BFO thin film (left) and nanocomposite BFO+CaF₂:Yb,Er (right). Excitation: 980 nm; emission: visible range (400-700 nm).

The images shown in Figure 54 highlight the difference between pure BFO, in which no luminescence is visible when irradiated by the 980 nm laser beam, and the BFO nanocomposite, containing UCNPs. For the BFO nanocomposite, the white pixels correspond to the emission from the sample, indicating that the upconversion emission from CaF₂ nanoparticles is observed in the nanocomposite. The microscope permits to acquire the emission in three separate spectral regions.

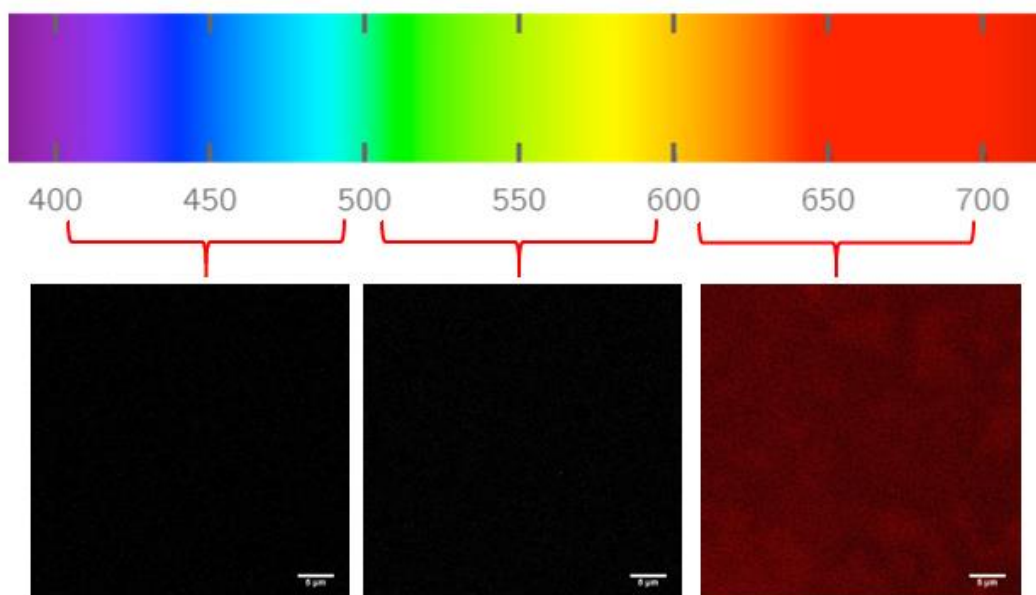


Figure 55. The acquisition of luminescence from the sample is divided into three different ranges, each one corresponding to a portion of the visible spectrum.

Figure 55 shows three images acquired for different spectral regions, 400-500 nm, 500-600 nm and 600-700 nm (see the upper part of the figure 55). It is clear that in the 400-600 nm range, no fluorescence is visible, while a homogeneous diffused emission has been observed in the 600-700 nm region, shown in red color in Figure 55 (third image). This luminescence is due to upconversion process of Er^{3+} ions (activators) around 650 nm, while the other emission of the Er^{3+} ions in the green region are not observed, as they fall within the absorption band of BFO. These results demonstrate that an energy transfer between the UCNPs and the ferroelectric photocatalyst could in principle be possible, as well as the possibility of extending the range of activation of the photoresponsive material.

5 CONCLUSIONS

Bismuth ferrite (BiFeO_3 , BFO) is a multiferroic material with interesting magnetic and electrical properties, it recently has attracted much interest due to its narrower band gap and to the photovoltaic and photocatalytic ability. Its band gap in the range 2.1-2.7 eV allows the absorption of visible light and this is very important because the visible light occupies about 48% of the total solar energy, while UV radiation only accounts for the 4%.

BFO could be synthesized with different method and in different sizes and shapes, such as nanoparticles, nanowires and it is generally known that size and morphology of the particles strongly affect the photoelectrocatalytic activity.

In this thesis work, BFO in thin films form has been prepared starting from a previously reported sol-gel method, optimizing synthetic parameters to find the optimal conditions for the formation of pure material. It has been found that the aging time of the precursor sol of BFO strongly affects the morphology and the PEC properties and maximum efficiency and homogeneity have been found depositing the material after five day of aging time, obtaining a highly nanostructured material, with particle size in the range 80-200 nm. This synthesis is quite simple and cheap, even though processing parameters have to be carefully controlled to obtain regular morphology and defect-free material with good photoelectrocatalytic efficiency.

To investigate the possibility to modify the structure and performance of BFO, a nanocomposite material has been developed, adding previously synthesized upconversion nanoparticles to the sol precursor of BFO and depositing the nanostructured thin films on FTO glass substrate.

The pure material and the nanocomposite have been characterized using several techniques and their performance have been compared. The modified BFO thin film nanocomposites show enhanced photoelectrocatalytic properties with a maximum production of photocurrent.

The increasing in photocurrent generation could be due to a distortion of crystalline structure or morphology of BFO nanomaterial, which increases the available surface area or the ferroelectric properties of the material.

Another interesting aspect is that the synthesis of nanocomposite material, such as BFO thin films doped with UCNPs, could be a strategy to broaden the range of radiation absorption to the NIR portion of electromagnetic radiation. In fact, NIR radiation constitutes the remaining ~50% of the sunlight radiation, but it is not utilized by the commonly used photocatalytic semiconductors and its low energy prevent it to be used for photocatalysis. Upconversion is an anti-Stokes process whereby two or more photons with lower energy, usually in the NIR range, excite energy levels of an atom and they are transformed in a photon at higher energy in the UV or visible range. Lanthanides possess energy levels making them optimal candidates for carrying out the UC process, although usually UC emission has low quantum yield.

To overcome these limitations and to increase the efficiency of UC, some strategies could be adopted in the future, such as the synthesis of inert shells around the luminescent core, to minimize the surface quenching or coupling the UCNPs with plasmonic metals and exploit the surface plasmon resonance (SPR) effect to increase the absorption of photons.³⁸

As a proof of concept, the upconversion emission from lanthanide-doped UCNPs has been investigated in the nanocomposite thin films using a multiphoton-confocal laser scanning microscope and emission between 600 and 700 nm has been found.

Further characterizations are needed on this material to understand the causes of morphological modification and the presence of energy transfer between the two materials.

Nevertheless, these results, together with the increasing of photoelectrocatalytic performance, has demonstrated the potential of such nanocomposite material and the possibility, not only to increase the performance by modifying the morphology, but also to harvest the part of the spectrum in the NIR region to exploit more and more the energy from solar radiation.

6 BIBLIOGRAPHY

- (1) El Chaar, L.; Lamont, L. A.; El Zein, N. Review of Photovoltaic Technologies. *Renew. Sustain. Energy Rev.* **2011**, *15* (5), 2165–2175.
- (2) Ellabban, O.; Abu-Rub, H.; Blaabjerg, F. Renewable Energy Resources: Current Status, Future Prospects and Their Enabling Technology. *Renew. Sustain. Energy Rev.* **2014**, *39*, 748–764.
- (3) Lianos, P. Review of Recent Trends in Photoelectrocatalytic Conversion of Solar Energy to Electricity and Hydrogen. *Appl. Catal. B Environ.* **2017**, *210*, 235–254.
- (4) Ahmad, H.; Kamarudin, S. K.; Minggu, L. J.; Kassim, M. Hydrogen from Photocatalytic Water Splitting Process: A Review. *Renew. Sustain. Energy Rev.* **2015**, *43*, 599–610.
- (5) Fujishima, A.; Honda, K. Electrochemical Photolysis of Water at a Semiconductor Electrode. *Nature* **1972**, *238* (5358), 37–38.
- (6) Wang, C.-C.; Li, J.-R.; Lv, X.-L.; Zhang, Y.-Q.; Guo, G. Photocatalytic Organic Pollutants Degradation In. *Energy Environ. Sci. Rev.* **2014**, *04*, 21322601.
- (7) Mahlambi, M. M.; Ngila, C. J.; Mamba, B. B. Recent Developments in Environmental Photocatalytic Degradation of Organic Pollutants: The Case of Titanium Dioxide Nanoparticles-A Review. *J. Nanomater.* **2015**, *2015* (October).
- (8) Hoffmann, M. R.; Martin, S. T.; Choi, W.; Bahnemann, D. W. Environmental Applications of Semiconductor Photocatalysis. *Chem. Rev.* **1995**, *95* (1), 69–96.
- (9) Zhang, L.; Webster, T. J. Nanotechnology and Nanomaterials: Promises for Improved Tissue Regeneration. *Nano Today* **2009**, *4* (1), 66–80.
- (10) Prasad, P. N. *Introduction to Nanomedicine and Nanobioengineering*; Wiley, Ed.; 2012.
- (11) Chen, G.; Roy, I.; Yang, C.; Prasad, P. N. Nanochemistry and Nanomedicine for Nanoparticle-Based Diagnostics and Therapy. *Chem. Rev.* **2016**, *116* (5), 2826–2885.

- (12) Pulickel M. Ajayan, Linda S. Schadler, P. V. B. *Nanocomposite Science and Technology*; Wiley, Ed.; 2003.
- (13) Labhassetwar, N.; Saravanan, G.; Kumar Megarajan, S.; Manwar, N.; Khobragade, R.; Doggali, P.; Grasset, F. Perovskite-Type Catalytic Materials for Environmental Applications. *Sci. Technol. Adv. Mater.* **2015**, *16* (3), 1–13.
- (14) Luo, J.; Im, J. H.; Mayer, M. T.; Schreier, M.; Nazeeruddin, M. K.; Park, N. G.; Tilley, S. D.; Fan, H. J.; Grätzel, M. Water Photolysis at 12.3% Efficiency via Perovskite Photovoltaics and Earth-Abundant Catalysts. *Science (80-.)*. **2014**, *345* (6204), 1593–1596.
- (15) Coey, J. M. D.; Viret, M. Mixed Valence Manganites. *Adv. Phys.* **2012**, *48* (1999), 167–293.
- (16) Nuraje, N.; Su, K. Perovskite Ferroelectric Nanomaterials. *Nanoscale* **2013**, *5* (19), 8752–8780.
- (17) Wang, J.; Neaton, J. B.; Zheng, H.; Nagarajan, V.; Ogale, S. B.; Liu, B.; Viehland, D.; Vaithyanathan, V.; Schlom, D. G.; Waghmare, U. V.; Spaldin, N. A.; Rabe, K. M.; Wuttig, M.; Ramesh, R. Epitaxial BiFeO₃ Multiferroic Thin Film Heterostructures. *Science (80-.)*. **2003**, *299* (5613), 1719–1722.
- (18) Gao, T.; Chen, Z.; Huang, Q.; Niu, F.; Huang, X.; Qin, L. A Review : Preparation of Bismuth Ferrite Nanoparticles and Its Applications in Visible-Light Induced Photocatalyses A REVIEW : PREPARATION OF BISMUTH FERRITE NANOPARTICLES AND ITS APPLICATIONS IN VISIBLE-LIGHT INDUCED PHOTOCATALYSES. **2015**, No. October.
- (19) Sajjadi, S. P. Sol-Gel Process and Its Application in Nanotechnology. *J. Polym. Eng. Technol.* **2005**, *13* (January), 38–41.
- (20) Zhang, Q.; Sando, D.; Nagarajan, V. Chemical Route Derived Bismuth Ferrite Thin Films and Nanomaterials. *J. Mater. Chem. C* **2016**, *4* (19), 4092–4124.
- (21) Carlos, L. D.; Palacio, F. *Thermometry at the Nanoscale: Techniques and Selected Applications*; RSC, 2014.

- (22) Bunzli, J. G.; Eliseeva, S. V. Basics of Lanthanide Photophysics. *Springer Ser. Fluoresc.* **2010**, *13* (July), 51–70.
- (23) Walsh, B. M. Judd-Ofelt Theory: Principles and Practices. *Adv. Spectrosc. Lasers Sens.* **2006**, 403–433.
- (24) Vetrone, F.; Capobianco, J. Lanthanide-Doped Fluoride Nanoparticles: Luminescence, Upconversion, and Biological Applications. *Int. J. Nanotechnol. - INT J NANOTECHNOL* **2008**, *5*.
- (25) Prodi, L.; Rampazzo, E.; Rastrelli, F.; Speghini, A.; Zaccheroni, N. Imaging Agents Based on Lanthanide Doped Nanoparticles. *Chem Soc Rev* **2015**, *44*, 4992.
- (26) Auzel, F. Upconversion and Anti-Stokes Processes with f and d Ions in Solids. *Chem. Rev.* **2004**, *104* (1), 139–173.
- (27) Arppe, R.; Hyppänen, I.; Perälä, N.; Peltomaa, R.; Kaiser, M.; Würth, C.; Christ, S.; Resch-Genger, U.; Schäferling, M.; Soukka, T. Quenching of the Upconversion Luminescence of NaYF₄:Yb³⁺,Er³⁺ and NaYF₄:Yb³⁺,Tm³⁺ Nanophosphors by Water: The Role of the Sensitizer Yb³⁺ in Non-Radiative Relaxation. *Nanoscale* **2015**, *7* (27), 11746–11757.
- (28) Deng, J.; Banerjee, S.; Mohapatra, S. K.; Smith, Y. R.; Misra, M. Bismuth Iron Oxide Nanoparticles as Photocatalyst for Solar Hydrogen Generation from Water. *J. Fundam. Renew. Energy Appl.* **2011**, *1*, 1–10.
- (29) Zhang, J.; Huang, Y.; Jin, L.; Rosei, F.; Vetrone, F.; Claverie, J. P. Efficient Upconverting Multiferroic Core@Shell Photocatalysts: Visible-to-Near-Infrared Photon Harvesting. *ACS Appl. Mater. Interfaces* **2017**, *9*, 8142–8150.
- (30) Hammond, C. *The Basics of Crystallography and Diffraction*, Fourth Edi.; Oxford Science Publications, 2015.
- (31) R.F. Egerton. *Physical Principles of Electron Microscopy*; 2005.
- (32) Tauc, J.; Grigorovici, R.; Vancu, A. Optical Properties and Electronic Structure of Amorphous Germanium. *pss-b* **1966**.
- (33) Hodes, G. Photoelectrochemical Cell Measurements: Getting the Basics Right. *J.*

- Phys. Chem. Lett.* **2012**, *3* (9), 1208–1213.
- (34) Ylmaz, P.; Yeo, D.; Chang, H.; Loh, L.; Dunn, S. Perovskite BiFeO₃ Thin Film Photocathode Performance with Visible Light Activity. *Nanotechnology* **27** (34), 1–9.
- (35) Cortelletti, P.; Pedroni, M.; Boschi, F.; Pin, S.; Ghigna, P.; Canton, P.; Vetrone, F.; Speghini, A.; Chimica, D.; Pavia, U.; Pavia, U.; Taramelli, V.; B, V. T. Luminescence of Eu³⁺ Activated CaF₂ and SrF₂ Nanoparticles: Effect of the Particle Size and Codoping with Alkaline Ions. **2018**.
- (36) Chen, J.; Xing, W.; Yun, Q.; Gao, W.; Nie, C.; Zhao, S. Effects of Ho, Mn Co-Doping on Ferroelectric Fatigue of BiFeO₃ Thin Films. *Electron. Mater. Lett.* **2015**, *11* (4), 601–608.
- (37) Dong, G.; Tan, G.; Luo, Y.; Liu, W.; Ren, H.; Xia, A. Investigation of Tb-Doping on Structural Transition and Multiferroic Properties of BiFeO₃ Thin Films. **2014**, *40*, 6413–6419.
- (38) Zhang, Q.; Yang, F.; Xu, Z.; Chaker, M.; Ma, D. Are Lanthanide-Doped Upconversion Materials Good Candidates for Photocatalysis? *Nanoscale Horizons* **2019**, *4* (3), 579–591.
- (39) Wikimedia Commons. Band Gap Comparison.